Cell

Molecular recognition of morphine and fentanyl by the human μ-opioid receptor

Graphical abstract

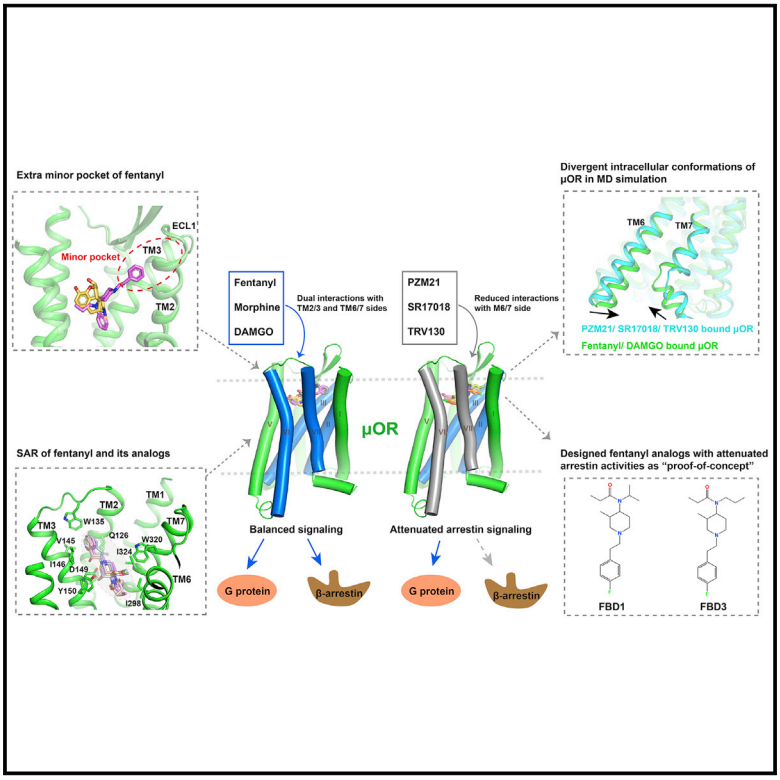

Highlights

- Structures of the human μOR bound to fentanyl, morphine, PZM21, TRV130, and SR17018
- Fentanyl occupies extra minor pocket around TM2 and TM3 beyond the morphine pocket
- Reduced ligand interaction with TM6/7 attenuates arrestin activity of μOR ligands
- Structure-based design of fentanyl analogs with reduced arrestin activities of μOR

Authors

Youwen Zhuang, Yue Wang, Bingqing He, ..., Ming-Wei Wang, Xin Xie, H. Eric Xu

Correspondence

zhuangyouwen@simm.ac.cn (Y.Z.), mwwang@simm.ac.cn (M.-W.W.), xxie@simm.ac.cn (X.X.), eric.xu@simm.ac.cn (H.E.X.)

In brief

Seeing how fentanyl, morphine, and other agonists bind and activate the μOR-G_i complex provides the basis for designing ligands with reduced arrestin signaling.

Zhuang et al., 2022, Cell *185*, 4361–4375
November 10, 2022
https://doi.org/10.1016/j.cell.2022.09.041

CellPress

Cell

CellPress

Article

Molecular recognition of morphine and fentanyl by the human μ-opioid receptor

Youwen Zhuang,[1,11,*] Yue Wang,[1,2,11] Bingqing He,[2,3,4,11] Xinheng He,[1,2,11] X. Edward Zhou,[5] Shimeng Guo,[2,3,6] Qidi Rao,[4] Jiaqi Yang,[1] Jinyu Liu,[6] Qingtong Zhou,[7] Xiaoxi Wang,[1] Mingliang Liu,[1] Weiyi Liu,[1,2] Xiangrui Jiang,[1,2] Dehua Yang,[1,2,3] Hualiang Jiang,[1,2,4] Jingshan Shen,[1,2] Karsten Melcher,[5] Hong Chen,[8,9] Yi Jiang,[1,2] Xi Cheng,[1,2] Ming-Wei Wang,[1,2,3,4,7,*] Xin Xie,[1,2,3,4,6,10,*] and H. Eric Xu[1,2,12,*]

[1]The CAS Key Laboratory of Receptor Research, Center for Structure and Function of Drug Targets, Shanghai Institute of Materia Medica, Chinese Academy of Sciences, Shanghai 201203, China

[2]University of Chinese Academy of Sciences, Beijing 100049, China

[3]The State Key Laboratory of Drug Research, The National Center for Drug Screening, Shanghai Institute of Materia Medica, Chinese Academy of Sciences, Shanghai 201203, China

[4]School of Life Science and Technology, ShanghaiTech University, Shanghai 201210, China

[5]Department of Structural Biology, Van Andel Research Institute, Grand Rapids, MI 49503, USA

[6]School of Chinese Materia Medica, Nanjing University of Chinese Medicine, Nanjing 210046, China

[7]Department of Pharmacology, School of Basic Medical Sciences, Fudan University, Shanghai 200032, China

[8]Shanghai Key Laboratory of Crime Scene Evidence, Shanghai Research Institute of Criminal Science and Technology, Shanghai 200083, China

[9]Shanghai Yuansi Standard Science and Technology Co., Ltd, Shanghai 200080, China

[10]School of Pharmaceutical Science and Technology, Hangzhou Institute for Advanced Study, UCAS, Hangzhou 310024, China

[11]These authors contribute equally

[12]Lead contact

*Correspondence: zhuangyouwen@simm.ac.cn (Y.Z.), mwwang@simm.ac.cn (M.-W.W.), xxie@simm.ac.cn (X.X.), eric.xu@simm.ac.cn (H.E.X.)

https://doi.org/10.1016/j.cell.2022.09.041

SUMMARY

Morphine and fentanyl are among the most used opioid drugs that confer analgesia and unwanted side effects through both G protein and arrestin signaling pathways of μ-opioid receptor (μOR). Here, we report structures of the human μOR-G protein complexes bound to morphine and fentanyl, which uncover key differences in how they bind the receptor. We also report structures of μOR bound to TRV130, PZM21, and SR17018, which reveal preferential interactions of these agonists with TM3 side of the ligand-binding pocket rather than TM6/7 side. In contrast, morphine and fentanyl form dual interactions with both TM3 and TM6/7 regions. Mutations at the TM6/7 interface abolish arrestin recruitment of μOR promoted by morphine and fentanyl. Ligands designed to reduce TM6/7 interactions display preferential G protein signaling. Our results provide crucial insights into fentanyl recognition and signaling of μOR, which may facilitate rational design of next-generation analgesics.

INTRODUCTION

Opioids are the most effective drugs for the treatment of acute and chronic pain, and they occupy the largest market share of analgesic medications. Opioids from poppy plant *Papaver somniferum* represent one of the most ancient plant-driven medications, whose usage as recreational and analgesic substances can be traced back to thousands of years ago (Brownstein, 1993). Medical uses of opioids for pain relief include opioid alkaloids and synthetic opioids, represented by morphine and fentanyl, two widely prescribed analgesics (Manglik, 2020). Although opioids are potent painkillers, they also result in severe adverse effects such as addiction, respiratory suppression, and constipation, thereby limiting their clinical utilization (Chan et al., 2017; Del Vecchio et al., 2017). Opioid overdose can cause death by respiratory suppression, which has led to a widely spread "opioid crisis," especially in Northern America. According to reports released in 2019, more than 70% deaths from opioid crisis were due to overdose of synthetic opioids, mainly fentanyl and its derivatives such as carfentanil and lofentanil (Mattson et al., 2021; Ringuette et al., 2020).

Functions of opioids are mediated by a family of four G protein-coupled receptors (GPCRs), namely μ, δ, κ, and nociception receptors (Al-Hasani and Bruchas, 2011; Waldhoer et al., 2004). Among these opioid receptors (ORs), μOR was revealed to be the main receptor for both the analgesic and adverse effects of morphine (Matthes et al., 1996). Signaling of μOR is primarily transduced through G_i to inhibit cAMP production. μOR can

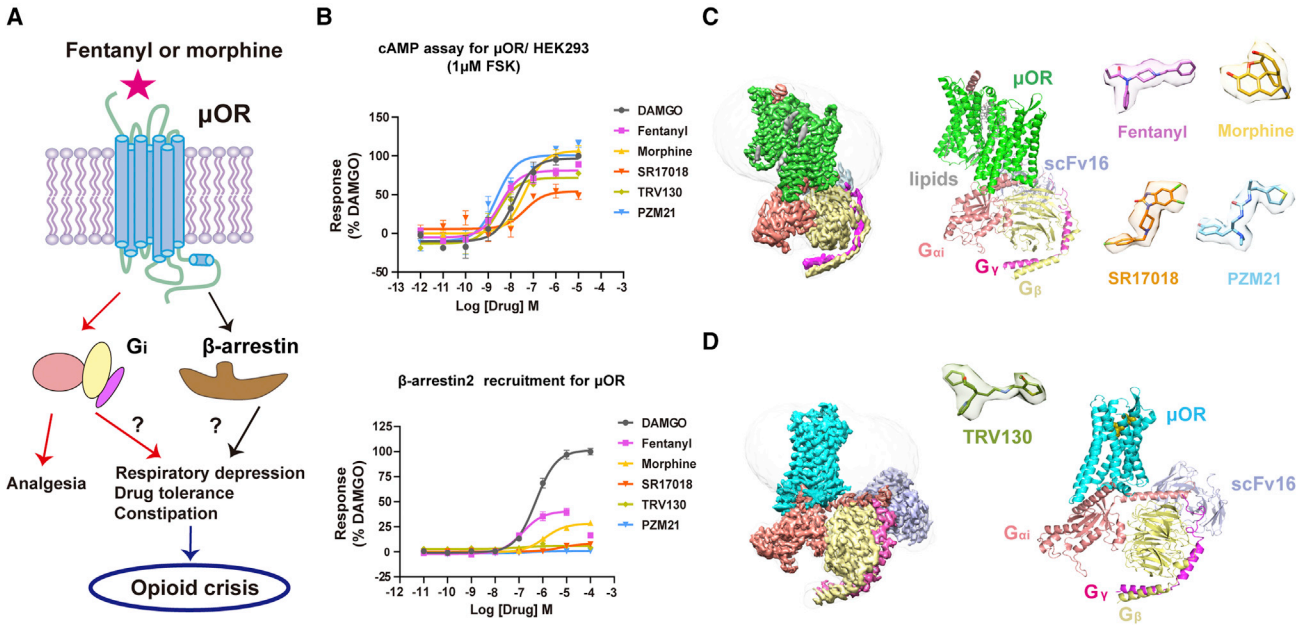

Figure 1. Cryo-EM structures of the human μOR-G_i signaling complexes

(A) Fentanyl and morphine induced μOR signaling and potential pharmacological effects.

(B) Dose-dependent response curves of opioid agonists, DAMGO, fentanyl, morphine, SR17018, TRV130, and PZM21. Responses shown are induced cAMP accumulations and β-arrestin 2 recruitments. Data were presented as means ± SEM with a minimum of three technical replicates, which were performed in triplicates each. The data were normalized according to the maximal response of DAMGO.

(C) Cryo-EM density map and molecular model of the fentanyl-μOR-G_i homodimer complex, and density maps of fentanyl (violet), morphine (gold), SR17018 (orange), and PZM21 (light cyan). The densities of ligands are shown in surface presentation and each ligand is shown in stick model. See Table S2.

(D) Structures of μOR-G_i complexes bound with TRV130. See Table S2.

See also Figures S1, S2, S3, and S4 and Table S1.

also signal through β-arrestin upon the receptor activation. It has been proposed that the opioid-induced analgesia is attributed to G_i signaling of μOR, whereas the unwanted side effects such as respiratory suppression and constipation might be caused by β-arrestin signaling (Bohn et al., 1999, 2000; Raehal et al., 2005). However, this proposal was challenged by recent findings, which suggest that the respiratory depression by opioids was due to G protein-gated inwardly rectifying potassium (GIRK) channel signaling and the opioid-induced severe side effects were independent of the β-arrestin pathway (Kliewer et al., 2019, 2020; Levitt et al., 2015; Montandon et al., 2016; Figure 1A). Despite the G protein-selective μOR agonist hypothesis being increasingly controversial, tremendous efforts have been made during the past decades to screen and develop μOR agonists with attenuated arrestin signaling activities, with the hope to find better analgesics with fewer side effects (Chan et al., 2017; Che et al., 2021). Several μOR agonists with negligible arrestin activities and potentially with better therapeutic windows than morphine and fentanyl have been identified and characterized, including oliceridine (TRV130), PZM21, and SR17018 (Chen et al., 2013; DeWire et al., 2013; Manglik et al., 2016; Schmid et al., 2017). Among them, oliceridine was approved by the US Food and Drug Administration (FDA) in 2020 for the treatment of moderate to severe pain, although the *in vivo* studies in rodents and clinical trials indicating that the side effects remained (Altarifi et al., 2017; Singla et al., 2019; Viscusi et al., 2019). For PZM21, different results and interpretations also existed regarding its efficacy, signaling preference, and effects on respiratory depression and tolerance (Hill et al., 2018; Manglik et al., 2016). It was suggested that the low efficacy in G protein pathway of the so-called biased ligands may explain their actions (Gillis et al., 2020). Detailed studies of ligands with various signaling properties would help to solve the above controversies. The signaling preference mechanism of μOR was investigated previously by methods including nuclear magnetic resonance (NMR) spectroscopy and computational simulations (Cong et al., 2021; de Waal et al., 2020; Hothersall et al., 2017). However, the structural understanding of such mechanism is still lacking, which largely limited the design of new ligands of μOR with signal preference.

Notable progresses have been made in structural studies of μOR, including crystal structures of the mouse μOR bound to its antagonist β-funaltrexamine (β-FNA) (Manglik et al., 2012) and agonist BU72 (Huang et al., 2015), both of which are modified morphine analogs with high affinity to μOR. Recently, a 3.5 Å cryoelectron microscopy (cryo-EM) structure of the mouse μOR-G_i complex bound to the peptidomimetic agonist Tyr-D-Ala-Gly-*N*-Me-Phe-Gly-ol (DAMGO) was also reported (Koehl et al., 2018). However, the structure of μOR in complex with fentanyl, the main cause of the opioid crisis, is still lacking. Fentanyl exhibits many aspects of abnormal pharmacology (Kelly et al., 2021), including the difficulty to be fitted into the binding pocket

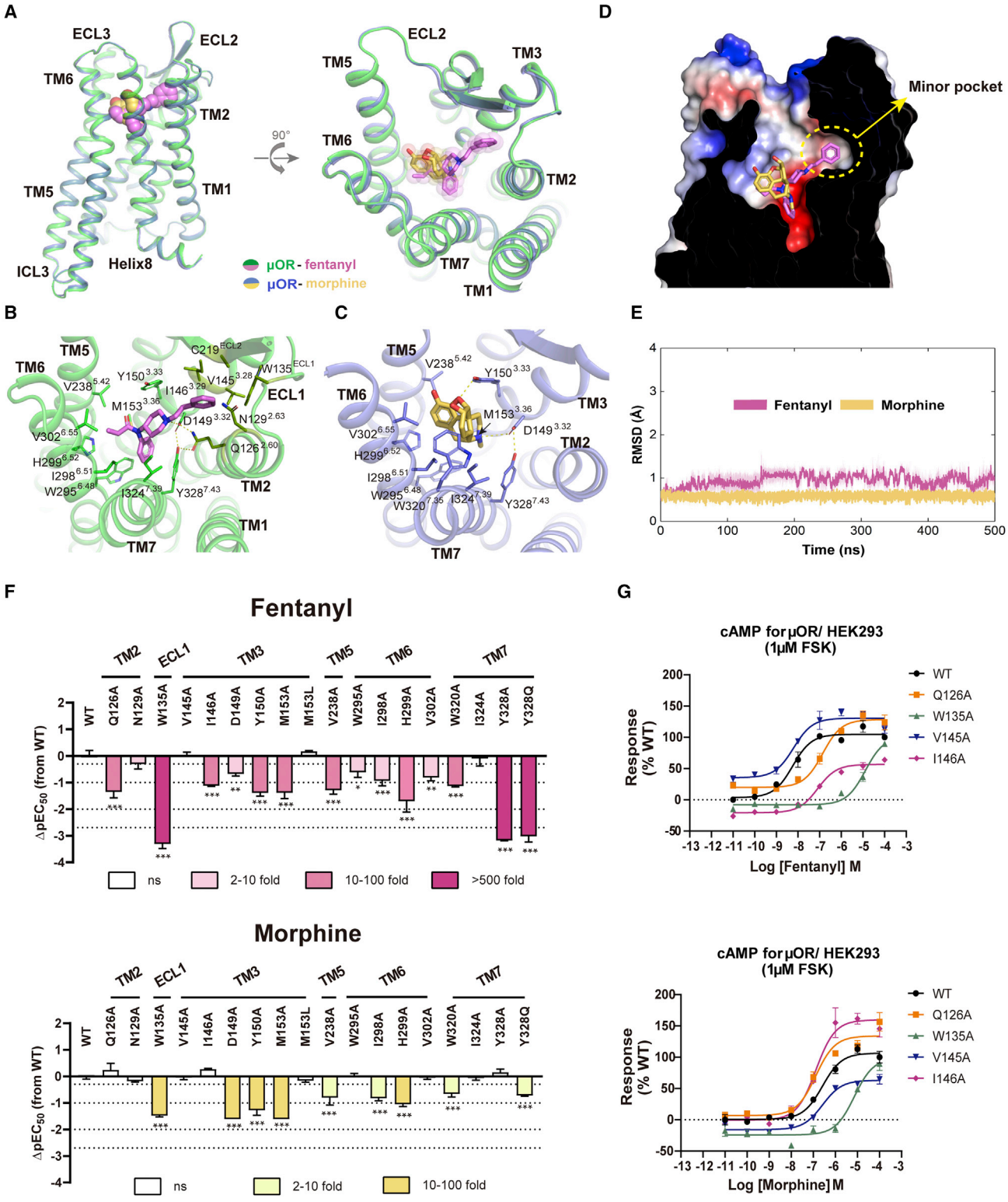

Figure 2. The ligand-binding modes of fentanyl and morphine

(A) Superimposition of fentanyl and morphine bound μOR structures.

(B and C) Interactions of fentanyl (B) and morphine (C) with μOR. The receptor portion is colored in green and blue in fentanyl and morphine bound μOR structures, respectively. Residues in the minor pocket are colored by dark green. Fentanyl: violet; morphine: gold.

(legend continued on next page)

of BU72 and DAMGO, which have completely different chemical scaffolds from fentanyl (de Waal et al., 2020; Eshleman et al., 2020; Lipiński et al., 2019; Ricarte et al., 2021; Vo et al., 2021). Intensive modeling efforts in fentanyl docking and simulation studies suggested many different binding modes, posing great challenges in understanding the structure-activity relationship (SAR) of numerous fentanyl derivatives (de Waal et al., 2020; Eshleman et al., 2020; Lipiński et al., 2019; Ricarte et al., 2021; Vo et al., 2021). Here, we report five cryo-EM structures of the human μOR-G_i complexes with morphine, fentanyl, SR17018, TRV130, and PZM21. These structures reveal distinct binding properties of morphine and fentanyl and the molecular determinants necessary for β-arrestin signaling of μOR. Based on these findings, we have designed fentanyl derivatives that showed largely attenuated or abolished β-arrestin activity while maintaining relatively intact G protein signaling compared with fentanyl.

RESULTS

Structure determination of μOR-G_i complexes

DAMGO and morphine are two well-studied μOR agonists activating both G protein and β-arrestin pathways, whereas fentanyl was proposed to be preferential to β-arrestin compared with the above two (Cong et al., 2021; Manglik et al., 2016; Schmid et al., 2017). We first characterized the signaling profiles of the six opioids with divergent chemical scaffolds used in this study: DAMGO, fentanyl, morphine, SR17018, TRV130, and PZM21 (Figure S1). We tested their effects on G protein signaling pathways using cAMP accumulation and $G_{i/o}$ recruitment assays, and their effects on β-arrestin pathways using β-arrestin recruitment assay. All five ligands could activate μOR to inhibit the production of cAMP, with fentanyl, morphine, and PZM21 acting as full agonists, whereas SR17018 and TRV130 being partial agonists when using DAMGO as reference in cAMP assay (Figure 1B). Nevertheless, in $G_{i/o}$ recruitment assay, PZM21, TRV130, and SR17018 all acted as μOR partial agonists (Figure S1C). The difference in G_i signaling efficacy of PZM21 resulting from different assays has been well acknowledged (Gillis et al., 2020; Hill et al., 2018; Manglik et al., 2016; Wang et al., 2022). Similar to previous studies (Manglik et al., 2016; Schmid et al., 2017; Wang et al., 2022), no response signals were detected for PZM21 in β-arrestin recruitment assays, whereas only weak signal was produced for SR17018 and TRV130 (Figures 1B, S1C, and S1D). In contrast, both morphine and fentanyl induced robust β-arrestin recruitments (Figures 1B, S1C, and S1D; Table S1).

To investigate the ligand-binding mode and signaling profiles of μOR, we used single particle cryo-EM to determine the structures of μOR-G protein complexes bound to fentanyl, morphine, SR17018, TRV130, and PZM21 (Figures 1C and 1D; Table S2). Interestingly, we observed that the μOR-G_i complexes with fentanyl, morphine, SR17018, and PZM21 appeared to exist as homodimers (Figure S1). Further negative staining imaging and cryo-EM structure determination of the μOR-G_i dimer indicated it to be an anti-parallel dimer, with the densities of two G proteins symmetrically distributed in opposite directions (Figures S2A and S2B).

The structures of μOR-G_i complexes with fentanyl, morphine, SR17018, TRV130, and PZM21 were determined with global nominal resolutions ranging from 2.8 to 3.3 Å (Figures S2 and S3). For each complex, the relatively high-resolution maps clearly showed most of the side chains and allowed us to model μOR from residues S66 to F352, including all three extracellular loops (ECLs) and three intracellular loops (ICLs) as well as helix 8 of μOR, the G_i heterotrimer without the flexible α-helical domain of $G_{\alpha i1}$, and scFv16 antibody. All ligands were clearly defined by the cryo-EM density maps (Figures 1C, 1D, and S4).

Specific binding of fentanyl and morphine to μOR

Morphine and fentanyl are two widely used opioids and differ from each other in chemical scaffolds. Morphine belongs to the family of benzylisoquinoline alkaloids with a morphinan scaffold, whereas fentanyl contains an anilinopiperidine moiety with a phenylethyl attached to the amine group of a piperidine ring (Figure S1B). The differences in chemical structures of morphine and fentanyl may elicit distinct conformational changes in the orthosteric binding pocket (OBP) of μOR. Indeed, despite the overall structures of μOR bound to these two ligands are highly similar (RMSD = 0.3 Å for the Cα atoms of μOR), their binding modes are quite different (Figures 2A–2D).

In our structure, the fentanyl molecule occupies a "Y" shaped conformation in the orthosteric pocket and contacts mainly with residues from TM2, TM3, TM6, and TM7 of transmembrane domain (TMD) (Figure 2B). The phenylethyl moiety faces toward the cleft of TM2 and TM3, and the propionyl group toward TM6, where it makes hydrophobic interactions with $I298^{6.51}$ and $V302^{6.55}$ (Ballesteros-Weinstein numbering; Ballesteros and Weinstein, 1995; Figures 2A and 2B). The n-aniline ring points downward to the core region of the TMD and forms a hydrophobic interaction network with residues $M153^{3.36}$, $W295^{6.48}$, $I298^{6.51}$, and TM7 residues $G327^{7.42}$ and $Y328^{7.43}$ (Figures 2A and 2B). Compared with fentanyl, morphine adopts an elliptical "O" configuration, interacting with hydrophobic residues from

(D) The minor pocket of μOR around TM2 and TM3 regions.

(E) Verification of fentanyl and morphine binding modes by 500-ns molecular dynamics simulation. The violet and gold lines show the RMSDs of all heavy atoms in fentanyl and morphine, respectively, during simulations. The shadow shows the standard error of 3 repeats.

(F) Decreases in G_i activation induced cAMP accumulation of μOR mutants activated by fentanyl (violet) and morphine (gold). The value of each column indicated differences in potency (ΔpEC_{50}) of representative μOR mutants relative to the WT μOR. All data are presented as means ± SEM with a minimum of three independent replicates performed in technical triplicate. See Tables S3–S5 for details. Data shown are means ± SEM from at least three independent experiments. The significance was determined with two-side, one-way ANOVA followed by Fisher's LSD multiple comparisons test compared with WT. *$p < 0.05$; **$p < 0.01$; and ***$p < 0.001$ were considered statistically significant.

(G) cAMP assays of WT and mutant μORs in the minor pocket activated by fentanyl (up) and morphine (down). Data are presented as means ± SEM with a minimum of three independent experiments and each in triplicate.

TM3, TM6, and TM7 (Figures 2A and 2C). The morphinan group overlaps with the propionyl group of fentanyl, with the hydroxyl of the phenol moiety of morphinan pointing toward TM5 (Figures 2A and 2C). Both the amine groups in the piperidine ring of fentanyl and in the morphinan group of morphine form salt bridges with the carboxylate group of D149$^{3.32}$ (Figures 2B and 2C), which is a universal interaction of ligands with opioid and bioamine receptors (Che et al., 2018; Claff et al., 2019; Granier et al., 2012; Huang et al., 2015; Manglik et al., 2012; Thompson et al., 2012; Vass et al., 2019). Similar to the BU72-μOR structure, D149$^{3.32}$ also forms polar interactions with nearby residues Q126$^{2.60}$ and Y328$^{7.43}$ (DQY polar motif, hereafter) in both structures (Figures 2B and 2C). The DQY motif is conserved among ORs. Consistent with κOR and δOR, mutations in the DQY polar motif, including D149$^{3.32}$A, Q126$^{2.60}$K, and Y328$^{7.43}$A, largely decreased potencies of both G protein and β-arrestin signaling of fentanyl and morphine, indicating that the DQY polar motif is crucial for μOR activation (Figures 2B and 2C; Tables S3–S5). Nevertheless, morphine is smaller and more compact than fentanyl and thus cannot form interactions equivalent to those mediated by the phenylethyl moiety and the n-aniline ring of fentanyl. The phenylethyl moiety of fentanyl occupies an extended hydrophobic minor pocket with residues from TM2 to TM3, including Q126$^{2.60}$ and W135^{ECL1} (Figure 2D). Molecular dynamics simulations reveal stable binding of fentanyl and morphine in the OBP of μOR with RMSD values at 0.5–1.5 Å from the poses determined by cryo-EM (Figure 2E). In addition, mutations of residues around the ligand-binding pockets of fentanyl and morphine, including Y150$^{3.33}$, M153$^{3.36}$, V238$^{5.42}$, I298$^{6.51}$, and H299$^{6.52}$, resulted in attenuated activities toward G protein and β-arrestin signaling of both ligands, further supporting their binding modes in each structure (Figure 2F; Tables S3–S5).

Fentanyl activates μOR 50–100 times more potently than morphine (Mather, 1983). Our structures provide a molecular basis for such potency difference. The benzene ring of fentanyl forms direct π-π interactions with the toggle switch residue W295$^{6.48}$ and Y328$^{7.43}$ (Figures 2B and 2C), which is absent in the morphine bound μOR structure. In addition, the phenylethyl moiety of fentanyl interacts hydrophobically with a minor pocket of μOR between TM2 and TM3, which is not occupied by morphine (Figures 2B–2D). Mutations on residues near the minor pocket, including Q126A, W135A, and I146A, affected more on fentanyl's potency than that of morphine (Figures 2F and 2G; Tables S3 and S4), indicating that the interaction in the minor pocket contributed to the higher potency of fentanyl to the receptor.

μOR activation by fentanyl and morphine

Comparisons of morphine or fentanyl bound μOR structures with that bound with the antagonist β-FNA shed light on the mechanism of μOR activation by morphine and fentanyl. Alignment of fentanyl and β-FNA bound structures reveals noticeable ligand induced conformational changes of μOR from the inactive to active states, including the twist of TM3, the inward movement of TM5, and the outward movement of TM6 in their intracellular parts, as well as clockwise rotations of TM2 and TM7 (Figure 3A). In the fentanyl bound μOR structure, the n-aniline ring formed a close π-π interaction with the toggle switch residue W295$^{6.48}$, resulting in a 28° shift of W295$^{6.48}$ toward F289$^{6.44}$ of the P$^{5.50}$I$^{3.40}$F$^{6.44}$ core triad (Figure 3B). The binding of fentanyl also caused twists of TM3 residues, especially from the D$^{3.32}$YYNM$^{3.36}$ motif. This leads to conformational changes of the DQY motif and I157$^{3.40}$ in the PIF triad, the collapse of the potential Na^+ pocket and the reconstruction of the water-mediated polar network containing residues D116$^{2.50}$, N152$^{3.35}$, S156$^{3.39}$, N330$^{7.45}$, and S331$^{7.46}$ (Figures 3B–3D). Similar to δOR (Claff et al., 2019), mutation of N152A in this polar network produced constitutive activation activity of μOR (Figures 3E and 3F). Moreover, compared with β-FNA, fentanyl adopted a pose facilitating the inward movement of TM5. The agonist induced inward movement of TM5 was demonstrated to be crucial for the activation of β_2-adrenergic receptor (β_2AR) and dopamine D1 receptor (D1R) (Rasmussen et al., 2011; Zhuang et al., 2021). Those conformational changes together lead to the rearrangement of PIF triad and NPxxY motif, the breaking of the ionic lock of the DRY motif, and the outward movement of TM6, opening the intercellular cavity for G protein coupling (Figure 3A). It is worth noting that both fentanyl and BU72 induced similar conformational changes of μOR, despite their different chemical scaffolds (Figures 3B–3D and S1B).

Morphine, which shares a morphinan core with BU72, adopted a nearly identical binding mode as BU72 and induced similar conformational changes of μOR as BU72 and fentanyl, including that in TM3 and TM5/6/7 (Figures 2A and 3A), indicating a common activation mechanism of these three agonists.

SAR of fentanyl and its derivatives

Fentanyl and its analogs, especially carfentanil, are key contributors of the opioid crisis. To understand the SAR of fentanyl derivatives, we docked carfentanil, lofentanil, sufentanil, remifentanil, and ohmefentanyl into the fentanyl-μOR structure. Consistent with their similar chemical scaffolds, fentanyl analogs share similar binding modes with that of fentanyl (Figures 4A–4G). Compared with fentanyl, carfentanil forms additional hydrophobic interactions with I298$^{6.51}$, W320$^{7.35}$, and I324$^{7.39}$ by the methoxycarbonyl group at the 4-position of the core piperidine ring (Figure 4C), which stabilize its binding to μOR and may explain its higher potency than fentanyl (Swanson et al., 2017). Sufentanil and remifentanil also make similar sets of hydrophobic interactions with TM6 and TM7, contributing to their higher affinity to μOR than fentanyl (Figures 4F and 4G). Mutations of I298A, W320A, and I324A showed much greater reduction of potencies of sufentanil and remifentanil than carfentanil, possibly due to their less extended hydrophobic interaction with the minor pocket compared with carfentanil (Figure 4H). Lofentanil is one of the most potent fentanyl derivatives with slightly higher affinity than carfentanil (Mather, 1983). In the docking model, lofentanil makes an extra *CH-π* interaction between the *cis*-methyl group of the piperidine ring and Y150$^{3.33}$ of μOR when compared with carfentanil (Figure 4D). Likewise, ohmefentanyl has an extra *cis*-methyl group in the piperidine ring like lofentanil and a hydroxyl group in the phenylethyl moiety, which could form additional *CH-π* and hydrogen bond interactions with Y150$^{3.33}$ and D149$^{3.32}$, respectively, thus explaining its 20 times higher potency than fentanyl (Figures 4E and 4I). Mutations of D149$^{3.32}$ and Y150$^{3.33}$ to alanine reduced the potency of ohmefentanyl

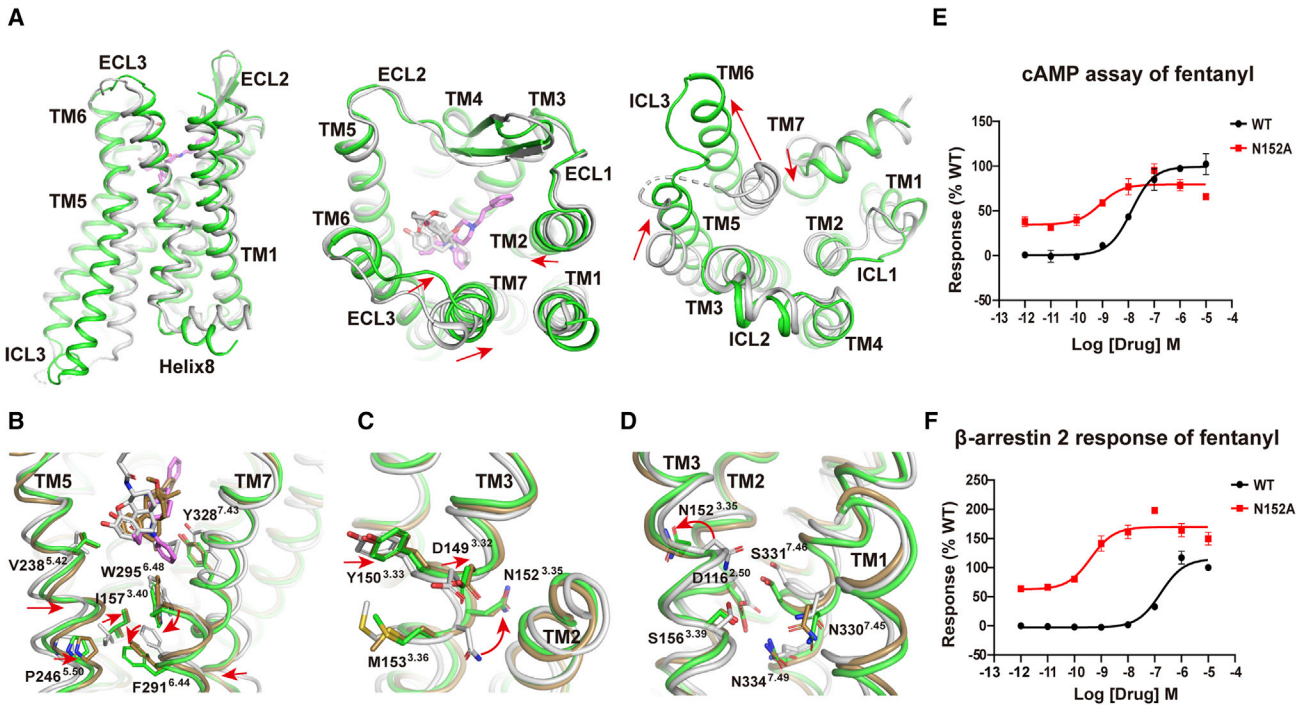

Figure 3. Fentanyl induced μOR activation

(A) Structure alignment of fentanyl activated μOR and antagonist (β-FNA) bound inactive μOR. Left: side view; middle: extracellular view; right: intracellular view. The conformational changes of fentanyl activated μOR compared with inactive μOR are marked with red arrows. The β-FNA-μOR structure (PDB: 4DKL) is colored in white; fentanyl and fentanyl-bound μOR are colored in violet and green, respectively.

(B–D) Conformational differences of important residues and motifs in μOR activation, including PIF triad (B), $D^{3.32}$YYNM$^{3.36}$ motif (C), and potential Na^+ pocket (D). Color usage: β-FNA-μOR (PDB: 4DKL), white; BU72-μOR (PDB: 5C1M), sand; fentanyl, violet; fentanyl bound μOR: green.

(E and F) Effects of N152A mutant in G_i activation (E) and β-arrestin 2 recruitment (F) of μOR. Data are presented as means ± SEM with a minimum of three independent experiments and each in triplicate.

more than that of fentanyl (Figures 4I and 4J), supporting the binding pose of ohmefentanyl in the docking model.

Structural determinants of β-arrestin signaling by μOR

As presented in Figures 1 and S1, SR17018, TRV130, and PZM21 are μOR agonists with very low or even abolished β-arrestin recruitment activity, thus showing preference for G protein signaling (Figures 1B, S1C, and S1D; Table S1). In contrast, fentanyl, morphine, and DAMGO display both G protein and arrestin recruitment activity. To understand the basis of the pharmacological profiles of these ligands, we obtained the structures of μOR bound with SR17018, TRV130, and PZM21. In our structures, all three ligands bind to μOR in OBP above W295$^{6.48}$ (Figure 5A), with their binding modes similar to each other. The benzimidazole ring of SR17018 and the methoxythiophen moiety of TRV130 and PZM21 bind to the minor pocket of μOR around TM2 and TM3 (Figure 5A). The chlorobenzene group of SR17018 points to TM6, whereas the oxaspiro moiety of TRV130 and the phenol group of PZM21 are oriented toward TM5 (Figure 5A). Similar to the n-aniline ring in fentanyl, the pyridine ring of TRV130 extends to the TMD core and forms close contacts with W295$^{6.48}$, G327$^{7.42}$, and Y328$^{7.43}$, which is absent in the SR17018- and PZM21-bound structures (Figure 5A).

We also obtained a structure of the human μOR bound with peptide agonist DAMGO at 3.3 Å (Figure S5A). The overall structure of the human μOR bound to DAMGO is similar to the previous 3.5 Å structure of the mouse μOR bound with DAMGO (Koehl et al., 2018) (RMSD at 0.7 Å for the Cα atoms of receptor), but with differences in helix 8, ECL2, and the binding pose at the C terminus of DAMGO (Figures S5B–S5F). In our structure, DAMGO adopts a similar binding mode compared with fentanyl, mainly interacting with residues from TM2/3 and TM6/7, with the phenylmethyl region of DAMGO occupying the minor pocket of TM2/3, the same pocket occupied by the phenylethyl moiety of fentanyl (Figures S5G and S5H; Table S4).

We conducted comprehensive structural comparisons of all six μOR structures determined in this study. Interestingly, we observed that both SR17018 and PZM21 adopted poses away from TM7 and had no direct interactions with TM7 residues (Figures 5B, 5C, and S6A–S6D). For SR17018, the pose of the piperidine ring moved about 1 Å away from TM7 to TM3 compared with that of fentanyl (Figure 5B). Alignment of PZM21 and DAMGO bound μOR structures showed that DAMGO generated additional interactions with TM7 through the D-alanine compared with PZM21 (Figure 5C). In addition to TM7, we also observed that both SR17018 and PZM21

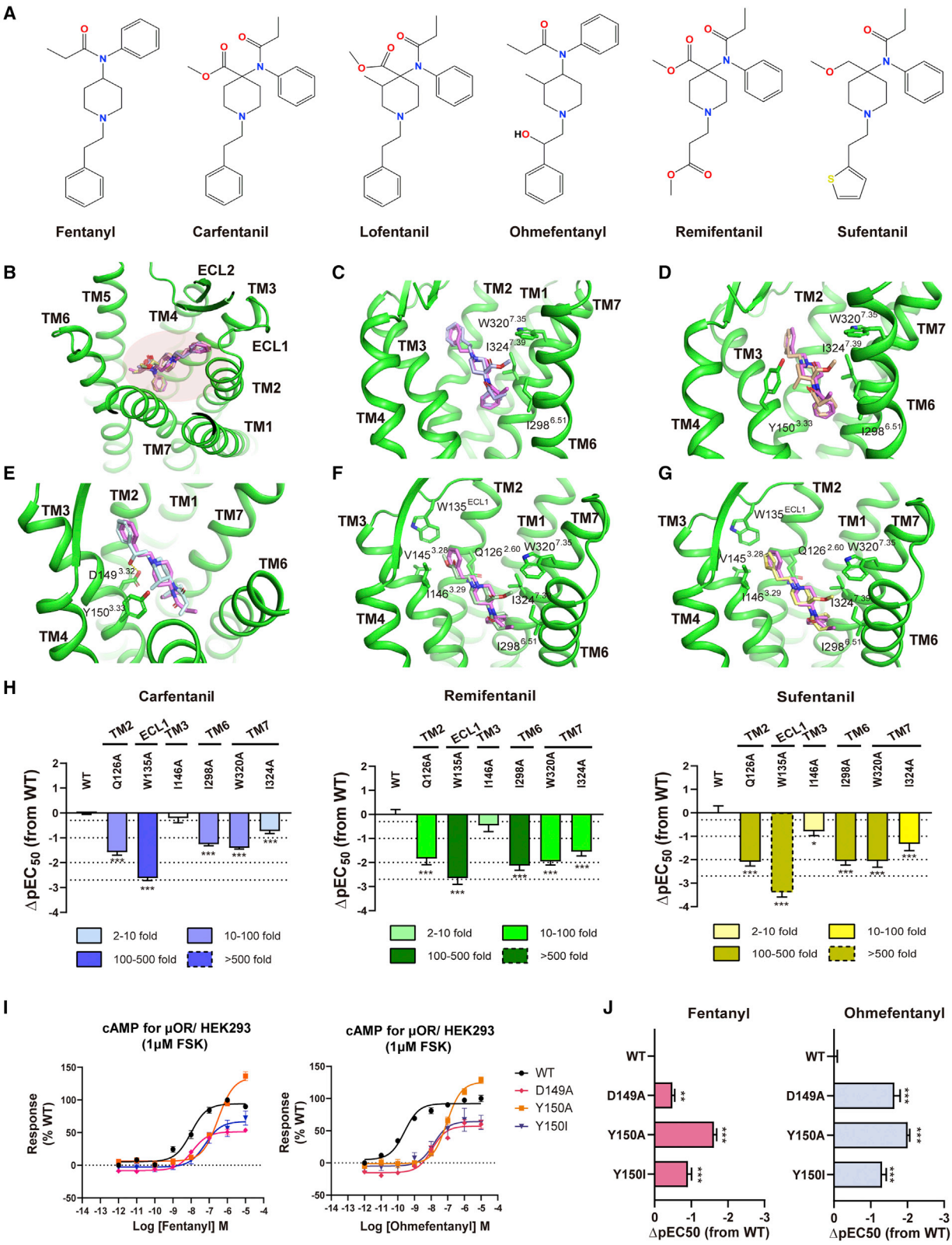

(legend on next page)

adopt only weak hydrophobic interactions with TM6 residues (Figures 5C and S6A–S6D). Molecular dynamics simulation results revealed that the binding of chlorobenzene of SR17018 is very flexible, suggesting the dynamic conformation of the chlorobenzene moiety near the TM6 region and unstable contact of SR17018 with TM6 of μOR (Figures S6E and S6F; Video S1). Since stable contacts with TM6 and TM7 were observed in μOR structures bound with DAMGO, fentanyl and morphine but not with SR17018 and PZM21, two ligands with nearly no arrestin recruitment activity (Figures S6E and S6F), we hypothesized that the reduced interactions of agonists with TM6 and TM7 might explain the pharmacology of SR17018 and PZM21. We thus mutated residues in the μOR OBP and tested the abilities of those mutants to activate G protein signaling and β-arrestin recruitment by fentanyl, morphine, and DAMGO, respectively. We found that mutations of residues near TM6 and TM7 showed more significant effects on β-arrestin signaling than those in TM2 and TM3 sides (Table S5). For instance, mutations W295A from TM6 and W320A from TM7 had only minimum or partial effects on G protein signaling in cAMP inhibition and G protein recruitment, whereas they nearly abolished the β-arrestin recruitment induced by fentanyl, morphine, and DAMGO (Figures 5D–5F and S6G–S6I; Tables S3–S5). Consistently, ligand interaction with $Y312^{7.35}$ of κOR, which corresponds to $W320^{7.35}$ of μOR, was demonstrated to be important for the β-arrestin signaling of κOR (Che et al., 2018). Additionally, mutations of I298A eliminated β-arrestin recruitment while having partial or minimum effects on G protein signaling of fentanyl and morphine (Figures 5D–5F and S6G–S6I; Tables S3–S5). Thus, stable interactions with TM6 and TM7 are necessary for β-arrestin signaling of μOR agonists.

Although TRV130 is a partial μOR agonist on G protein pathway, it maintains very weak β-arrestin signaling ability, with much lower efficacy than that of fentanyl. In our structures, TRV130 adopts a similar binding pose as SR17018 and PZM21, with the exception that the pyridine ring of TRV130 forms extra hydrophobic interactions with TM6/7 (Figures 5A, S6A–S6D, S7A, and S7B). Nevertheless, the binding modes of TRV130 and fentanyl could be well superimposed. The exception is that the pyridine ring of TRV130 tilted 35° toward TM2 relative to the n-aniline group of fentanyl (Figure 5A). This resulted in weaker hydrophobic interactions with TM6/7 than fentanyl, which may explain the weak β-arrestin signaling ability of TRV130 (Figures 5A and S7A).

Divergent intracellular conformations of μOR agonists

Agonists with different binding poses and pharmacological profiles may elicit distinct effects on the μOR intracellular part, which eventually leads to different coupling profiles of G protein and β-arrestin. To investigate the intracellular conformational variations of μOR upon binding of different opioid ligands, we conducted MD simulations of the μOR structures bound to SR17018, TRV130, and PZM21, three ligands with negligible β-arrestin activities. The opioid agonists with strong β-arrestin activity, such as fentanyl and DAMGO, were used as references. The tendency reflected that intracellular sides of TM6 and TM7-H8 in DAMGO and fentanyl systems moved toward the TM core, especially for the TM7-H8 junction, thus squeezed the intracellular cavity and decreased both solvent accessible surface area (SASA) and the volume of μOR intracellular pocket (Figures 6A and 6B). In contrast, the SASA and volume of μOR intracellular regions in SR17018, TRV130, and PZM21 bound systems were similar with those in μOR-G protein complexes (~2,622 $Å^2$ and ~1,456 $Å^3$, respectively), inferring more exposure of pocket residues and different preference for G protein and β-arrestin (Figure 6A).

To further elucidate the relationship of the observed intracellular conformation differences with β-arrestin coupling, we constructed μOR-β-arrestin models based on MD structures and two different GPCR-β-arrestin structures (M_2 muscarinic acetylcholine receptor (M_2R)-β-arrestin1, Protein Data Bank [PDB]: 6U1N [Staus et al., 2020]; neurotensin receptor type 1 (NTSR1)-β-arrestin1, PDB: 6UP7 [Huang et al., 2020]) and investigate the compatibility of β-arrestin and conformations induced by different ligands. In fentanyl and DAMGO bound structure models, the inwardly moved TM6 and TM7-H8 of μOR led to much more contracted intracellular pockets and broader interaction interface areas with β-arrestin, facilitating the interactions between β-arrestin and μOR (Figures 6B and 6C). In contrast, in SR17018, TRV130, and PZM21 bound structure models, the intracellular TM6 and TM7-H8 parts of μOR tended to be away from the TM core, which decreased the μOR-β-arrestin interaction interface and weakened its ability for β-arrestin binding (Figures 6B and 6C). Our simulation results are consistent with the previous cryo-EM and MD studies, which suggested that the ligands preferential to β-arrestin signaling induced a narrower GPCR intracellular conformation suitable for stable β-arrestin coupling of $β_1$ adrenergic receptor ($β_1$AR) and angiotensin II type 1 receptor (AT_1R) (Lee et al., 2020b; Wingler et al., 2019). Collectively, our MD simulations showed that the μOR agonists with G protein signaling preference

Figure 4. Molecular docking and characterization of fentanyl derivatives

(A) Chemical structures of fentanyl and its five analogs.

(B) Alignment of binding poses of fentanyl and its analogs in orthosteric binding pocket (OBP) of μOR. All five fentanyl analogs adopt similar poses as fentanyl. The ligand-binding region is circled.

(C–G) Structural comparisons of the fentanyl-μOR structure with carfentanil (C), lofentanil (D), ohmefentanyl (E), remifentanil (F), and sufentanil (G) bound μOR structures, respectively. The specific differences in interactions with μOR are shown. Color usage: fentanyl, violet; carfentanil, light blue; lofentanil, wheat; ohmefentanyl, light cyan; remifentanil, light green; sufentanil, light yellow. The μOR is colored in green.

(H) Validation of carfentanil, remifentanil, and sufentanil binding poses by cAMP accumulation assays. Data were presented as means ± SEM with a minimum of three independent replicates performed in technical triplicate. *$p < 0.05$; **$p < 0.01$, and ***$p < 0.001$ by one-way ANOVA followed by Fisher's LSD multiple comparisons test compared with WT.

(I and J) Effects of $D149^{3.32}$ and $Y150^{3.33}$ on the potencies of fentanyl and ohmefentanyl. cAMP analysis of the WT μOR and D149A and Y150A mutants induced by fentanyl and ohmefentanyl, respectively. The dose-response curves (I) and pEC_{50} values of the mutants relative to WT, i.e., ΔpEC_{50} (J), were presented. Data shown are means ± SEM from at least three independent experiments and each in triplicate. The significance was determined with two-side, one-way ANOVA followed by Fisher's LSD multiple comparisons test compared with WT. *$p < 0.05$; **$p < 0.01$, and ***$p < 0.001$ were considered statistically significant.

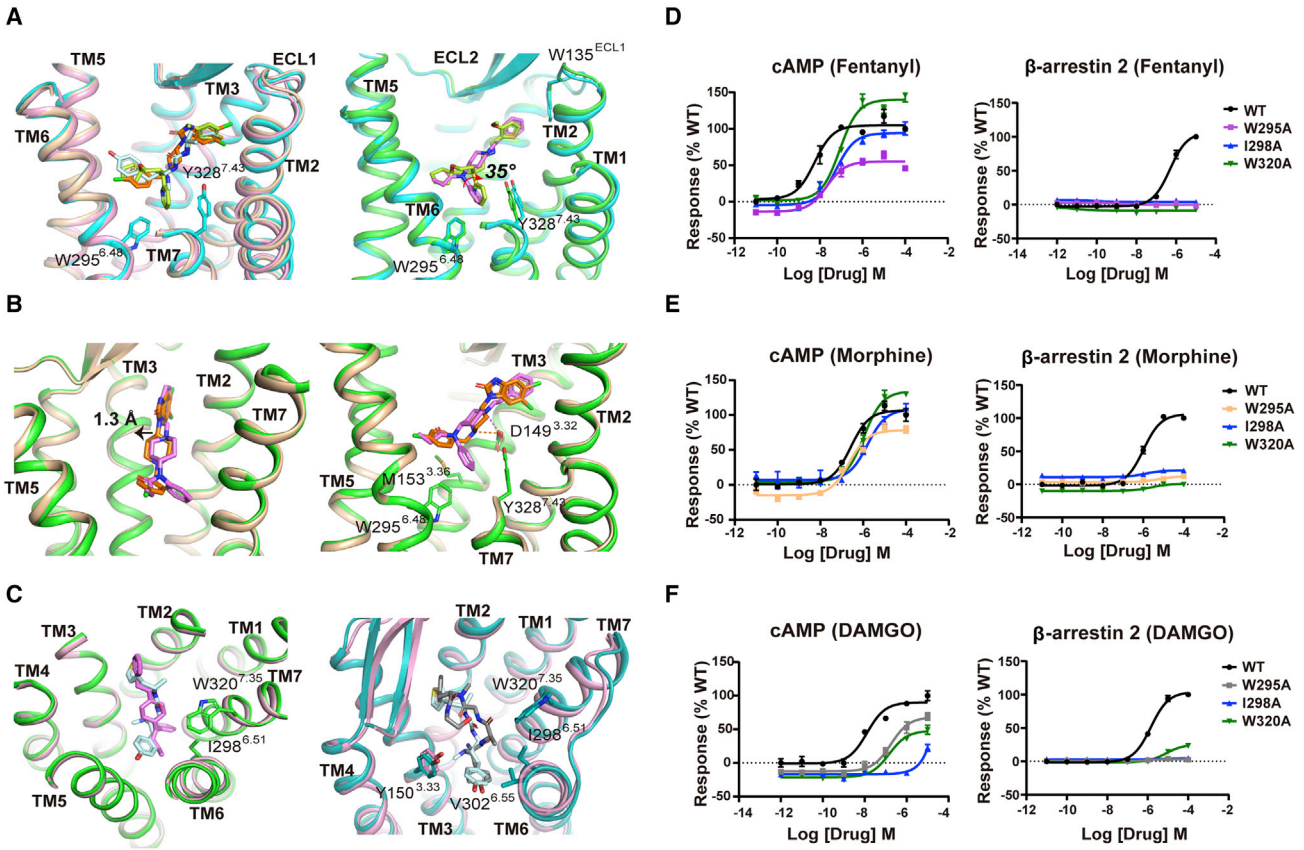

Figure 5. Determinants of β-arrestin signaling of μOR

(A) Comparisons of binding modes of SR17018, PZM21, and TRV130 (left) and TRV130 and fentanyl (right). The pyridine ring of TRV130 tilted 35° away from $W295^{6.48}$ relative to the n-aniline ring of fentanyl. Color usage: SR17018, orange; PZM21, light cyan; TRV130, olive; and fentanyl, violet. The receptor portions of SR17018, PZM21, TRV130, and fentanyl bound μOR structures were colored in wheat, pink, cyan, and green, respectively.

(B) Differences in the binding poses between SR17018 and fentanyl (left) and the specific interactions of μOR with fentanyl in the TMD core relative to SR17018 (right). SR17018 adopted a pose away from TM6/7 and toward the TM3 side. Color usage: SR17018, orange; fentanyl, violet. The receptor portions of SR17018, and fentanyl bound μOR structures were colored in wheat and green, respectively.

(C) Superimposition of the PZM21-μOR structure with the fentanyl-μOR (left) structure or DAMGO-μOR structure (right). Similar to SR17018, PZM21 shifted away from TM6/7. The methyl group in tertiary amine of PZM21 formed *CH-π* interaction with $Y150^{3.33}$, which was absent in the DAMGO-μOR structure. Color usage: PZM21, light cyan; fentanyl, violet; and DAMGO, gray. The receptor parts of PZM21, fentanyl, and DAMGO bound μOR structures are colored in wheat, green, and teal, respectively.

(D–F) Mutations of representative residues in TM6/7 moderately affected cAMP responses, yet abolished the arrestin recruitments induced by fentanyl (D), morphine (E), and DAMGO (F). Data were presented as means ± SEM with a minimum of three technical replicates, which were performed in triplicates each. See also Figures S5, S6, S7A, and S7B and Tables S3–S5.

maintained the μOR intracellular pocket similar to that of μOR-G protein structure, whereas the ligands that are neutral toward G protein and β-arrestin signaling induced inward movement of intracellular TM6 and TM7-H8, leading to different intracellular conformations suitable for stable coupling of β-arrestin. Since the stable contact between ligands and μOR in TM6-TM7 leads to β-arrestin signaling, it can be inferred that extended interactions with TM6-TM7 may elicit inward movement of TM6 and TM7-H8 toward the TM core, leading to enhancement of β-arrestin coupling.

Structure-based design of fentanyl analogs with reduced β-arrestin activities

To further validate our discovery that ligand interaction with TM6/7 contributes to β-arrestin signaling of μOR, we rationally designed fentanyl derivatives to reduce TM6/7 interaction, with the aim to obtain μOR agonists with reduced/abolished β-arrestin signaling but relatively intact G protein activity. We use propyl or isopropyl groups to replace the n-aniline moiety in fentanyl, which form interactions with TM6/7. We also induced a *cis*-methyl group to the piperidine ring and a para-fluorine to the phenylethyl moiety of fentanyl, leading to two structurally similar compounds, FBD1 and FBD3 (Figure 7A). Both propyl and isopropyl substituents are smaller than the n-aniline moiety, weakening the interactions of designed drugs with TM6/7 of μOR. Indeed, both FBD1 and FBD3 showed great reduction in β-arrestin recruitment activities in reference to fentanyl. Especially, FBD3 showed nearly identical potency and efficiency as fentanyl in either cAMP inhibition or G_i recruitment assays but had very limited β-arrestin

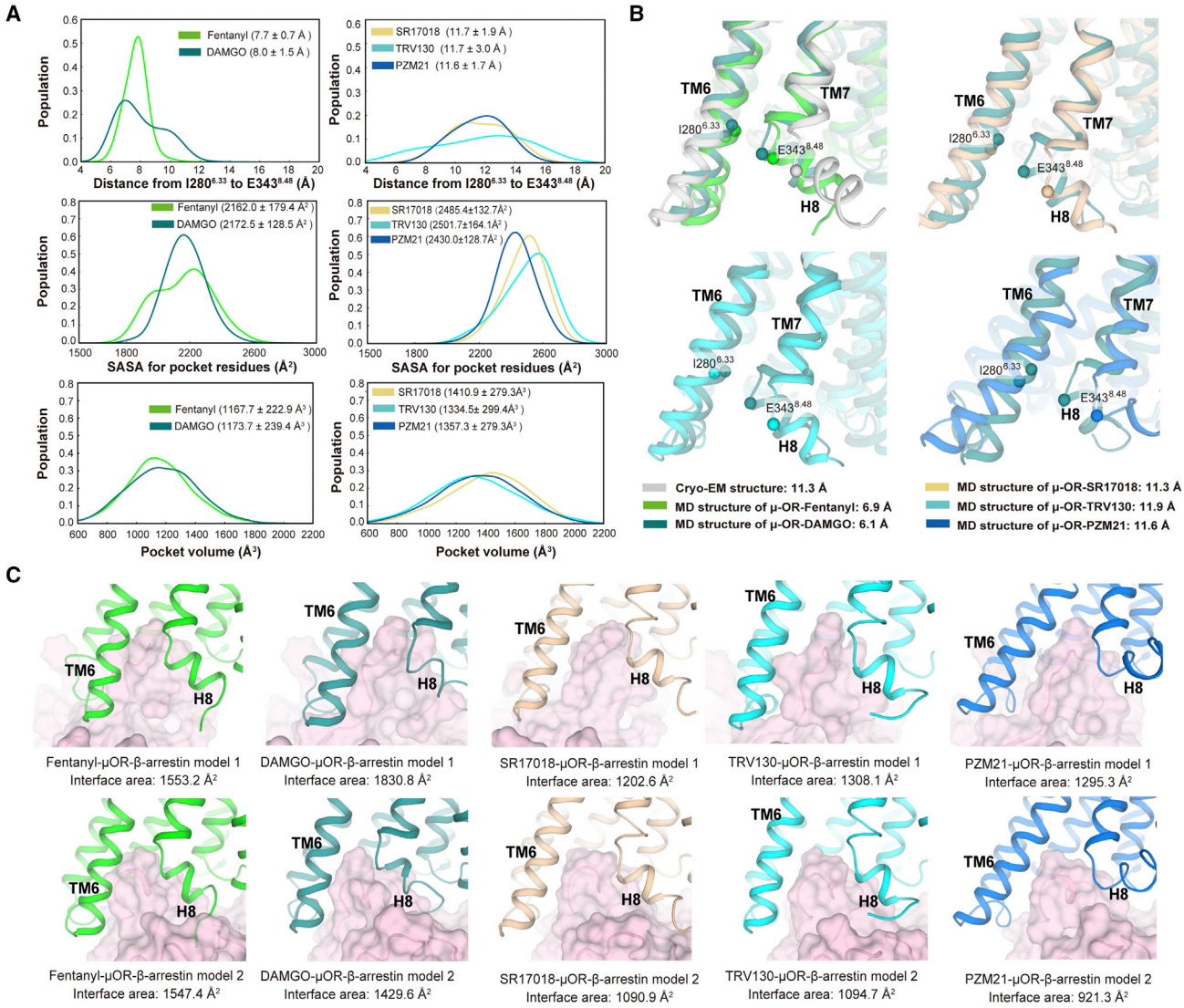

Figure 6. Conformational changes of intracellular part by divergent ligands in MD

(A) The distribution of C-alpha distance between I280$^{6.33}$ and E343$^{8.48}$, SASA for pocket residues, and pocket volume for μOR-fentanyl, DAMGO, SR17018, TRV130, and PZM21 systems. The average value and standard deviation for each system were also shown.

(B) The TM6-H8 conformation in cryo-EM structure, and each representative structure within specific distance ranges in MD trajectories. C-alphas of I280$^{6.33}$ and E343$^{8.48}$ were shown in spheres. The distance values are shown below.

(C) The β-arrestin models based on MD representative structures. During model construction, M_2R-β-arrestin 1 (PDB: 6U1N, for model 1) and NTSR1-β-arrestin 1 (PDB: 6UP7, for model 2) were aligned to MD representative structures and the complexes encountered minimization to be suitable. μOR and β-arrestin were shown as cartoon and surface, respectively. The interface area was shown below each complex. Color usage: cryo-EM structure, gray; MD structure of μOR-fentanyl, green; MD structure of μOR-DAMGO, teal; MD structure of μOR-SR17018, wheat; MD structure of μOR-TRV130, cyan; and MD structure of μOR-PZM21, blue.

See also Figure S6.

recruitment activity (Figures 7B and 7C; Table S6). Molecular docking showed that FBD1 and FBD3 adopt similar binding poses in μOR OBP, with the exception that the propyl substituent of FBD3 inserted more deeply into the pocket compared with isopropyl, thereby leading to potential hydrophobic interactions with residues from TM6 and TM7, including W295$^{6.48}$ and Y328$^{7.43}$ (Figures 7D and 7E). Thus, these two ligands served as a "proof-of-concept" that the effect of ligand interaction with TM6/7 is critical in eliciting arrestin signaling by μOR and that reducing this interaction may result in ligand signaling preferentially via the G protein pathway (Figure 7F).

DISCUSSION

Fentanyl and its analogs constitute the main causes of the "opioid crisis"; however, the mode of their binding to μOR remains a

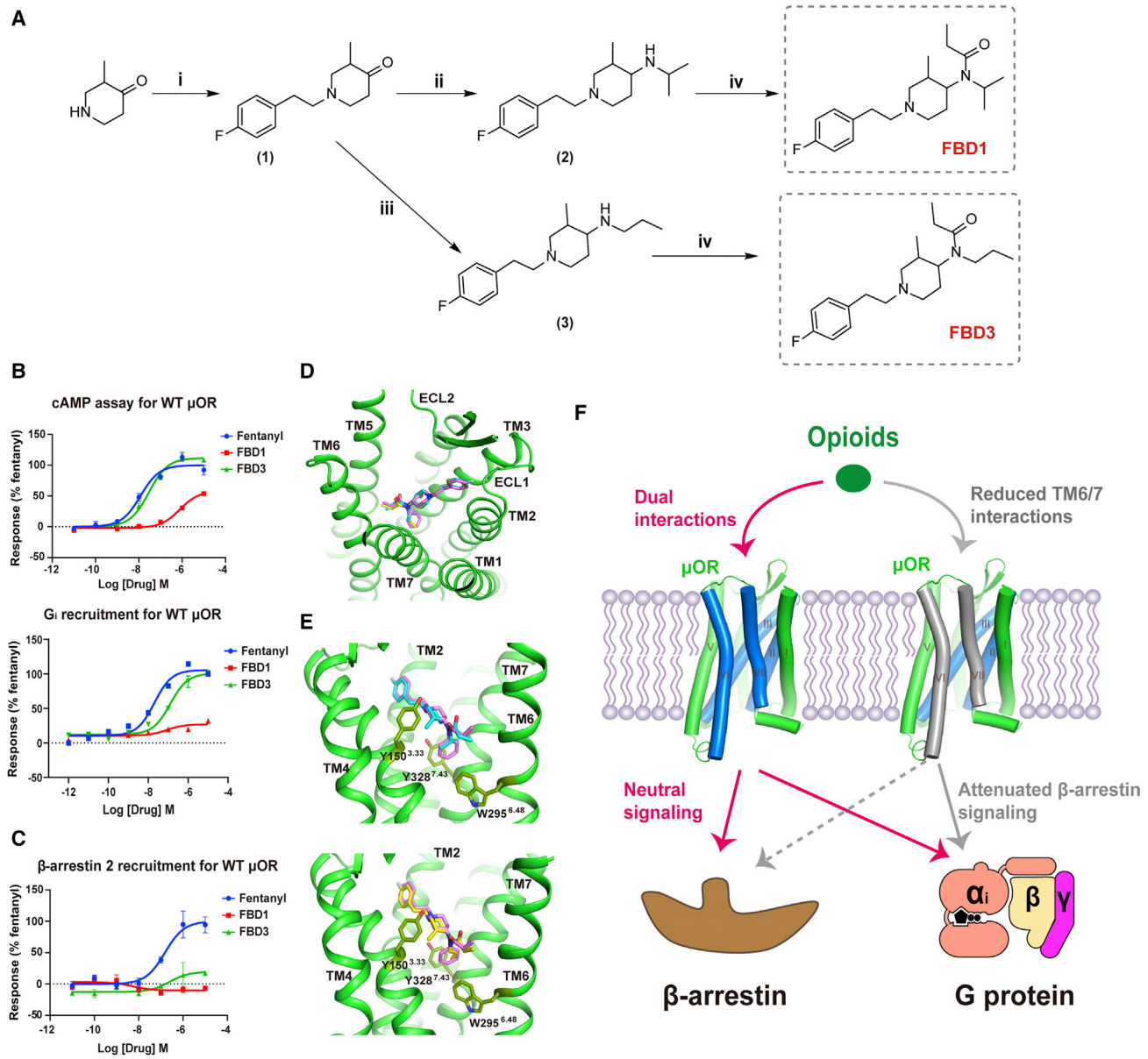

Figure 7. Design of fentanyl-derived μOR agonists

(A) Synthesis of fentanyl derivatives FBD1 and FBD3. i, Cs_2CO_3, ACN, 80°C; ii, isopropylamine, AcOH, $NaBH(OAc)_3$, 0°C to RT; iii, propylamine, AcOH, $NaBH(OAc)_3$, DCM, 0°C to RT; and iv, propionyl chloride, DIPEA, DCM, 0°C. (1), 1-(4-Fluorophenethyl)-3-methylpiperidin-4-one; (2), 1-(4-fluorophenethyl)-N-isopropyl-3-methylpiperidin-4-amine; and (3), 1-(4-fluorophenethyl)-3-methyl-N-propylpiperidin-4-amine.

(B) Dose-response curves of cAMP accumulation assay (up) and G_i recruitment (down) of FBD1 and FBD3 with fentanyl as reference ligand. FBD3 is a full agonist like fentanyl, and FBD1 is a partial agonist in both G protein recruitment and cAMP assays. The pEC_{50} of cAMP responses of FBD1 and FBD3 are 6.11 ± 0.08 and 7.53 ± 0.08, respectively. The pEC_{50} of G_i recruitment responses of FBD1 and FBD3 are 7.08 ± 0.39 and 6.90 ± 0.10, respectively. Data are presented as means ± SEM with a minimum of three independent experiments and each in triplicate. See Table S6 for details.

(C) β-Arrestin 2 recruitment of FBD1 and FBD3 with fentanyl as the reference ligand. FBD3 shows robustly decreased β-arrestin 2 recruitment activity. No β-arrestin 2 recruitment response is detected for FBD1, while the pEC_{50} of β-arrestin 2 recruitment of FBD3 is 6.60 ± 0.46. See Table S6 for details.

(D) Alignment of the fentanyl-μOR structure with the docking poses of FBD1 and FBD3. μOR, green; fentanyl, violet; FBD1, cyan; and FBD3, yellow.

(E) Comparison of the binding modes of fentanyl with that of FBD1 (up) and FBD3 (down), respectively. μOR, green; fentanyl, violet; FBD1, cyan; and FBD3, yellow.

(F) A cartoon model of ligand induced divergent signaling properties of μOR. The neutral signaling toward both G protein and β-arrestin is induced when opioid ligands, such as fentanyl, form broad interactions with most of the TMD regions of μOR, including TM2/3 and TM6/7. Nevertheless, the reduced arrestin signaling is conducted when opioid ligands, such as fentanyl derivatives FBD1 and FBD3, show reduced interactions with TM6/7 but preferred interactions with TM3 side of the orthosteric binding pocket.

See also Figure S6.

challenging problem. We presented the structure of fentanyl bound μOR, which reveals a specific fentanyl binding mode and provides a rational model for understanding SAR of extensive fentanyl derivatives in the literature (Burns et al., 2018; de Waal et al., 2020). The binding mode of fentanyl in our structure differs from the prior computational modeling studies (Ricarte et al., 2021; Vo et al., 2021), which did not identify the conformations of the tertiary amine group and phenylethyl moiety. In our structures, fentanyl adopts a distinct binding pose from those of morphine and DAMGO, with fentanyl forming extended interactions with the TMD core via the n-aniline ring, leading to a close contact with the toggle switch $W^{6.48}$. In addition, fentanyl occupies an extra hydrophobic minor pocket near the TM2/3 region when compared with morphine, partially accounting for its higher potency than morphine.

Fentanyl and its derivatives, such as carfentanil, lofentanil, and sufentanil, share a similar chemical scaffold but differ from each other in side-chain substituents of piperidine core and n-aniline moiety. Consistently, the docking poses of these fentanyl derivatives exhibit high similarities with the fentanyl binding pose, with only differences in the interactions of distinct side-chain substituents with μOR. Given their structure similarity, the fentanyl derivatives might activate μOR by a similar mechanism as fentanyl, and our results provide a unified recognition pattern to design safer fentanyl analogs with better pharmacological profiles.

Our structures also provide the basis to explain the selectivity of fentanyl and its analogs for μOR over κOR and δOR, despite the only subtle differences in residue composition in the OBPs of these three ORs (Figure S7C). Alignment of fentanyl-bound μOR and active δOR structures indicates that residue differences at $W320^{7.35}$L and $N129^{2.63}$K from μOR to δOR contribute to its lower affinity to fentanyl, with $W320^{7.35}$L leading to a much more open OBP and $N129^{2.63}$K being energetically unfavorable to the binding of the hydrophobic phenylethyl moiety of fentanyl to δOR (Figure S7D). For κOR, the inward movements of TM2/6 and ECL1 from μOR to κOR induce a steric clash with fentanyl, with the side chain of $Q115^{2.60}$ in κOR pushing away the tertiary amine of fentanyl, explaining the lower potency of fentanyl toward κOR (Figure S7E).

Finally, understanding the molecular basis of preferential signaling mechanism has remained a challenging task. In this paper, we have reported six structures of μOR bound to three agonists of neutral signaling profile (morphine, fentanyl, and DAMGO) and three agonists with reduced β-arrestin signaling activities (SR17018, TRV130, and PZM21). Analyses of these structures have revealed that all neutral agonists form stable interactions with both sides of the OBP formed by TM2/3 and TM6/7, whereas the SR17018, TRV130, and PZM21 showed only preferred interactions with the TM2/3 side of pocket and no/weak interactions with TM6/7 (Figure 7F). In our experiments, mutations that interfere with TM6/7 interactions, especially residues $W295^{6.48}$ and $W320^{7.35}$, largely diminished or abolished arrestin signaling, although they had limited influence on G protein activation by neutral agonists, including DAMGO. Our data are consistent with those of previous reports that corresponding TM7 residue $Y^{7.35}$ of κOR serves as structural determinant of β-arrestin activity (Che et al., 2018). Additionally, residues in TM6/7 were demonstrated to be important for the preferred G protein activation of D1R (Zhuang et al., 2021), 5-hydroxytryptamine receptor 2B ($5HT_{2B}R$) (McCorvy et al., 2018), sphingosine-1-phosphate receptor 1 (S1PR1) (Xu et al., 2022), and C-C motif chemokine receptor 1 (CCR1) (Shao et al., 2022), similar to that of μOR revealed in this study. Thus, we proposed that the structural determinants required for arrestin signaling of μOR uncovered in this study may be compatible to other GPCRs, especially for the other ORs considering their high structural similarities (Che et al., 2018), and phylogenetically close neighbors of μOR, like somatostatin and chemokine receptors (Shao et al., 2022). Together, our results reveal molecular details of the structural factors important for arrestin activity of μOR and provide structural templates for the design of potent and potentially safer analgesia for pain treatment.

Limitations of the study

In this study, by determining the cryo-EM structures of μOR-G_i complexes activated by ligands with different signal profiles, in combination with mutagenesis studies, we not only revealed the specific binding modes of morphine, fentanyl, and fentanyl derivatives but also uncovered the structural determinants, i.e., the TM6 and TM7 side of the OBP, that is critical for β-arrestin signaling of μOR. Ligands show less or no interaction with this motif display clearly reduced β-arrestin activation. Since these are G protein stabilized structures, the G protein certainly overwhelms the effects of the ligands on the intracellular side of the receptor. Thus, the signaling process leading to β-arrestin recruitment from the binding of fentanyl, morphine, and DAMGO remain to be answered. We also conducted extended investigations on the intracellular conformations of μOR induced by arrestin-attenuated and signaling-neutral agonists using molecular dynamic simulation of the determined structures without G protein. We found that the TM6 and TM7-helix 8 region of the receptor displayed different conformations while binding to arrestin-attenuated or signaling-neutral ligands, indicating that these motifs may contribute to β-arrestin signaling. The further modeling study suggested that the inward movement of TM6 and TM7-H8 regions in fentanyl and DAMGO bound μOR models led to much more contracted intracellular pockets to facilitate β-arrestin binding, in contrast to a wider open intracellular region induced by agonists with attenuated β-arrestin signaling. However, simulation modeling would not be accurate enough to study the subtle conformational dynamics in preferential signaling. It was also suggested that different μOR agonists, even with similar pharmacological profiles, induced divergent GPCR kinase (GRK)-mediated phosphorylation states at the C terminus of the receptor, which was linked with their β-arrestin activities (Gillis et al., 2020; Kliewer et al., 2019). Further studies, including structural studies on μOR complexed with GRK or β-arrestin, would be necessary to clarify how reduced TM6/7 interactions leads to different intracellular conformations, thus causing different coupling effects of μOR to G protein versus β-arrestin.

STAR★METHODS

Detailed methods are provided in the online version of this paper and include the following:

- KEY RESOURCES TABLE
- RESOURCE AVAILABILITY

SUPPLEMENTAL INFORMATION

Supplemental information can be found online at https://doi.org/10.1016/j.cell.2022.09.041.

ACKNOWLEDGMENTS

The cryo-EM data were collected at the Cryo-Electron Microscopy Research Center, Shanghai Institute of Materia Medica (SIMM) and Advanced Center for Electron Microscopy, Shanghai Institute of Materia Medica (SIMM). This work was partially supported by grants from the Ministry of Science and Technology (China) (2018YFA0507000 to M.-W.W. and 2018YFA0507002 to H.E.X.), National Natural Science Foundation of China (82121005 to X.X., H.E.X., Y.J., and D.Y.; 32130022 to H.E.X.; 81730099 to X.X.; 81872915 and 82073904 to M.-W.W.; 32171187 to Y.J.; 81773792 and 81973373 to D.Y.; and 21704064 to Q.Z.), the Shanghai Municipal Science and Technology Major Project (2019SHZDZX02 to H.E.X.), the CAS Strategic Priority Research Program (XDB37030103 to H.E.X.), Shanghai Municipal Science and Technology Major Project (H.E.X.), National Science & Technology Major Project of China-Key New Drug Creation and Manufacturing Program (2018ZX09735-001 to M.-W.W. and 2018ZX09711002-002-005 to D.Y.), and the Special Research Assistant Project of Chinese Academy of Sciences (to Y.Z.).

AUTHOR CONTRIBUTIONS

H.E.X. and Y.Z. initiated the project. Y.Z. designed and screened the expression constructs of μOR; optimized the protein complexes purification conditions; prepared protein samples of morphine, fentanyl, SR17018, and PZM21 bound μOR-G_i-scFv16 complexes toward cryo-EM data collection; prepared and screened the cryo-EM grids; and performed data acquisition and structure determination of morphine, fentanyl, and SR17018 bound μOR-G_i-scFv16 complexes. Y.Z. designed the fentanyl derivatives FBD1 and FBD3. Y.W. prepared protein samples of TRV130 bound μOR-G_i-scFv16 complex for cryo-EM data collection and determined the structures of TRV130-μOR-G_i-scFv16 and PZM21-μOR-G_i-scFv16 complexes, performed data acquisition and structure determination of PZM21 and TRV130 bound μOR-G_i-scFv16 complexes, participated in cAMP and arrestin recruitment assays, and characterized the activities of FBD1 and FBD3 by cAMP and arrestin recruitment assays. Q.R. prepared protein samples and performed cryo-EM data acquisition of DAMGO-μOR-G_i-scFv16 complex. Q.Z. determined the structure of DAMGO-μOR-G_i-scFv16 complex. B.H. and S.G. performed most of the mutagenesis studies and functional assays, analyzed the data, and prepared related figures and methods. S.G. performed arrestin recruitment assays and functional data analysis and participated in cAMP assays. J.Y. and M.L. synthesized compounds FBD1 and FBD3. J.L. assisted in cAMP assays and arrestin recruitment assays. X.H. performed molecular dynamics simulation and docking assays and participated in method editing and figure preparation. X.E.Z. modeled and refined all structures. X.W. and W.L. assisted in protein sample preparation. X.J. and H.C. assisted in compounds preparation and synthesis. J.S. supervised X.J. in compound synthesis. Y.J. supervised X.W. in protein sample preparation. K.M. supervised X.E.Z. and participated in manuscript editing. X.X. supervised pharmacological and mutagenesis experiments and participated in manuscript editing. M.-W.W. and D.Y. supervised Q.R. and Q.Z. and participated in manuscript editing. X.C. and H.J. supervised X.H. in computational work. H.E.X. conceived and supervised the project and participated in manuscript editing. Y.Z. prepared the draft of the manuscript. H.E.X. and Y.Z. wrote the manuscript.

DECLARATION OF INTERESTS

The authors declare no competing interests.

Received: December 15, 2021
Revised: June 30, 2022
Accepted: September 26, 2022
Published: November 10, 2022

REFERENCES

Adams, P.D., Afonine, P.V., Bunkóczi, G., Chen, V.B., Davis, I.W., Echols, N., Headd, J.J., Hung, L.W., Kapral, G.J., Grosse-Kunstleve, R.W., et al. (2010). Phenix: a comprehensive Python-based system for macromolecular structure solution. Acta Crystallogr. D Biol. Crystallogr. *66*, 213–221.

Al-Hasani, R., and Bruchas, M.R. (2011). Molecular mechanisms of opioid receptor-dependent signaling and behavior. Anesthesiology *115*, 1363–1381.

Altarifi, A.A., David, B., Muchhala, K.H., Blough, B.E., Akbarali, H., and Negus, S.S. (2017). Effects of acute and repeated treatment with the biased Mu Opioid receptor agonist TRV130 (oliceridine) on measures of antinociception, gastrointestinal function, and abuse liability in rodents. J. Psychopharmacol. *31*, 730–739.

Ballesteros, J.A., and Weinstein, H. (1995). Integrated methods for the construction of three-dimensional models and computational probing of structure-function relations in G protein-coupled receptors. Methods Neurosci. *25*, 366–428.

Bohn, L.M., Gainetdinov, R.R., Lin, F.T., Lefkowitz, R.J., and Caron, M.G. (2000). Mu-opioid receptor desensitization by beta-arrestin-2 determines morphine tolerance but not dependence. Nature *408*, 720–723.

Bohn, L.M., Lefkowitz, R.J., Gainetdinov, R.R., Peppel, K., Caron, M.G., and Lin, F.T. (1999). Enhanced morphine analgesia in mice lacking beta-arrestin 2. Science *286*, 2495–2498.

Brownstein, M.J. (1993). A brief history of opiates, opioid peptides, and opioid receptors. Proc. Natl. Acad. Sci. USA *90*, 5391–5393.

Burns, S.M., Cunningham, C.W., and Mercer, S.L. (2018). DARK classics in chemical neuroscience: fentanyl. ACS Chem. Neurosci. *9*, 2428–2437.

Chan, H.C.S., McCarthy, D., Li, J., Palczewski, K., and Yuan, S. (2017). Designing safer analgesics via mu-opioid receptor pathways. Trends Pharmacol. Sci. *38*, 1016–1037.

Che, T., Dwivedi-Agnihotri, H., Shukla, A.K., and Roth, B.L. (2021). Biased ligands at opioid receptors: current status and future directions. Sci. Signal. *14*, eaav0320.

Che, T., Majumdar, S., Zaidi, S.A., Ondachi, P., McCorvy, J.D., Wang, S., Mosier, P.D., Uprety, R., Vardy, E., Krumm, B.E., et al. (2018). Structure of the nanobody-stabilized active state of the kappa Opioid receptor. Cell *172*, 55–67.e15.

Chen, V.B., Arendall, W.B., 3rd, Headd, J.J., Keedy, D.A., Immormino, R.M., Kapral, G.J., Murray, L.W., Richardson, J.S., and Richardson, D.C. (2010). MolProbity: all-atom structure validation for macromolecular crystallography. Acta Crystallogr. D Biol. Crystallogr. *66*, 12–21.

Chen, X.T., Pitis, P., Liu, G., Yuan, C., Gotchev, D., Cowan, C.L., Rominger, D.H., Koblish, M., Dewire, S.M., Crombie, A.L., et al. (2013). Structure-activity relationships and discovery of a G protein biased Mu Opioid receptor ligand, [(3-methoxythiophen-2-yl)methyl]({2-[(9R)-9-(pyridin-2-yl)-6-oxaspiro-[4.5] decan- 9-yl]ethyl})amine (TRV130), for the treatment of acute severe pain. J. Med. Chem. *56*, 8019–8031.

Claff, T., Yu, J., Blais, V., Patel, N., Martin, C., Wu, L., Han, G.W., Holleran, B.J., Van der Poorten, O., White, K.L., et al. (2019). Elucidating the active delta-opioid receptor crystal structure with peptide and small-molecule agonists. Sci. Adv. *5*, eaax9115.

Cong, X., Maurel, D., Déméné, H., Vasiliauskaité-Brooks, I., Hagelberger, J., Peysson, F., Saint-Paul, J., Golebiowski, J., Granier, S., and Sounier, R. (2021). Molecular insights into the biased signaling mechanism of the mu-opioid receptor. Mol. Cell *81*, 4165–4175.e6.

de Waal, P.W., Shi, J., You, E., Wang, X., Melcher, K., Jiang, Y., Xu, H.E., and Dickson, B.M. (2020). Molecular mechanisms of fentanyl mediated beta-arrestin biased signaling. PLoS Comput. Biol. *16*, e1007394.

Del Vecchio, G., Spahn, V., and Stein, C. (2017). Novel opioid analgesics and side effects. ACS Chem. Neurosci. *8*, 1638–1640.

DeWire, S.M., Yamashita, D.S., Rominger, D.H., Liu, G., Cowan, C.L., Graczyk, T.M., Chen, X.T., Pitis, P.M., Gotchev, D., Yuan, C., et al. (2013). A G protein-biased ligand at the mu-opioid receptor is potently analgesic with reduced gastrointestinal and respiratory dysfunction compared with morphine. J. Pharmacol. Exp. Ther. *344*, 708–717.

Duan, J., Shen, D.D., Zhou, X.E., Bi, P., Liu, Q.F., Tan, Y.X., Zhuang, Y.W., Zhang, H.B., Xu, P.Y., Huang, S.J., et al. (2020). Cryo-EM structure of an activated VIP1 receptor-G protein complex revealed by a NanoBiT tethering strategy. Nat. Commun. *11*, 4121.

Emsley, P., and Cowtan, K. (2004). Coot: model-building tools for molecular graphics. Acta Crystallogr. D Biol. Crystallogr. *60*, 2126–2132.

Eshleman, A.J., Nagarajan, S., Wolfrum, K.M., Reed, J.F., Nilsen, A., Torralva, R., and Janowsky, A. (2020). Affinity, potency, efficacy, selectivity, and molecular modeling of substituted fentanyls at opioid receptors. Biochem. Pharmacol. *182*, 114293.

Gillis, A., Gondin, A.B., Kliewer, A., Sanchez, J., Lim, H.D., Alamein, C., Manandhar, P., Santiago, M., Fritzwanker, S., Schmiedel, F., et al. (2020). Low intrinsic efficacy for G protein activation can explain the improved side effect profiles of new opioid agonists. Sci. Signal. *13*, eaaz3140.

Granier, S., Manglik, A., Kruse, A.C., Kobilka, T.S., Thian, F.S., Weis, W.I., and Kobilka, B.K. (2012). Structure of the delta-opioid receptor bound to naltrindole. Nature *485*, 400–404.

He, X., Man, V.H., Yang, W., Lee, T.S., and Wang, J. (2020). A fast and high-quality charge model for the next generation general AMBER force field. J. Chem. Phys. *153*, 114502.

Heydenreich, F.M., Vuckovic, Z., Matkovic, M., and Veprintsev, D.B. (2015). Stabilization of G protein-coupled receptors by point mutations. Front. Pharmacol. *6*, 82.

Hill, R., Disney, A., Conibear, A., Sutcliffe, K., Dewey, W., Husbands, S., Bailey, C., Kelly, E., and Henderson, G. (2018). The novel mu-opioid receptor agonist PZM21 depresses respiration and induces tolerance to antinociception. Br. J. Pharmacol. *175*, 2653–2661.

Hothersall, J.D., Torella, R., Humphreys, S., Hooley, M., Brown, A., McMurray, G., and Nickolls, S.A. (2017). Residues W320 and Y328 within the binding site of the mu-opioid receptor influence opiate ligand bias. Neuropharmacology *118*, 46–58.

Huang, W., Manglik, A., Venkatakrishnan, A.J., Laeremans, T., Feinberg, E.N., Sanborn, A.L., Kato, H.E., Livingston, K.E., Thorsen, T.S., Kling, R.C., et al. (2015). Structural insights into micro-opioid receptor activation. Nature *524*, 315–321.

Huang, W., Masureel, M., Qu, Q., Janetzko, J., Inoue, A., Kato, H.E., Robertson, M.J., Nguyen, K.C., Glenn, J.S., Skiniotis, G., et al. (2020). Structure of the neurotensin receptor 1 in complex with beta-arrestin 1. Nature *579*, 303–308.

Jo, S., Cheng, X., Lee, J., Kim, S., Park, S.J., Patel, D.S., Beaven, A.H., Lee, K.I., Rui, H., Park, S., et al. (2017). CHARMM-GUI 10 years for biomolecular modeling and simulation. J. Comput. Chem. *38*, 1114–1124.

Kelly, E., Sutcliffe, K., Cavallo, D., Ramos-Gonzalez, N., Alhosan, N., and Henderson, G. (2021). The anomalous pharmacology of fentanyl. Br J Pharmacol. https://doi.org/10.1111/bph.15573.

Kliewer, A., Gillis, A., Hill, R., Schmiedel, F., Bailey, C., Kelly, E., Henderson, G., Christie, M.J., and Schulz, S. (2020). Morphine-induced respiratory depression is independent of beta-arrestin2 signalling. Br. J. Pharmacol. *177*, 2923–2931.

Kliewer, A., Schmiedel, F., Sianati, S., Bailey, A., Bateman, J.T., Levitt, E.S., Williams, J.T., Christie, M.J., and Schulz, S. (2019). Phosphorylation-deficient G-protein-biased mu-opioid receptors improve analgesia and diminish tolerance but worsen opioid side effects. Nat. Commun. *10*, 367.

Koehl, A., Hu, H., Maeda, S., Zhang, Y., Qu, Q., Paggi, J.M., Latorraca, N.R., Hilger, D., Dawson, R., Matile, H., et al. (2018). Structure of the micro-opioid receptor-Gi protein complex. Nature *558*, 547–552.

Kucukelbir, A., Sigworth, F.J., and Tagare, H.D. (2014). Quantifying the local resolution of cryo-EM density maps. Nat. Methods *11*, 63–65.

Lee, J., Cheng, X., Swails, J.M., Yeom, M.S., Eastman, P.K., Lemkul, J.A., Wei, S., Buckner, J., Jeong, J.C., Qi, Y., et al. (2016). CHARMM-GUI input generator for NAMD, GROMACS, AMBER, OpenMM, and CHARMM/OpenMM simulations using the CHARMM36 additive force field. J. Chem. Theor. Comput. *12*, 405–413.

Lee, J., Hitzenberger, M., Rieger, M., Kern, N.R., Zacharias, M., and Im, W. (2020a). CHARMM-GUI supports the Amber force fields. J. Chem. Phys. *153*, 035103.

Lee, Y., Warne, T., Nehmé, R., Pandey, S., Dwivedi-Agnihotri, H., Chaturvedi, M., Edwards, P.C., García-Nafría, J., Leslie, A.G.W., Shukla, A.K., et al. (2020b). Molecular basis of beta-arrestin coupling to formoterol-bound beta1-adrenoceptor. Nature *583*, 862–866.

Levitt, E.S., Abdala, A.P., Paton, J.F., Bissonnette, J.M., and Williams, J.T. (2015). Mu Opioid receptor activation hyperpolarizes respiratory-controlling Kolliker-Fuse neurons and suppresses post-inspiratory drive. J. Physiol. *593*, 4453–4469.

Lipiński, P.F.J., Jarończyk, M., Dobrowolski, J.C., and Sadlej, J. (2019). Molecular dynamics of fentanyl bound to mu-opioid receptor. J. Mol. Model. *25*, 144.

Liu, P., Jia, M.Z., Zhou, X.E., De Waal, P.W., Dickson, B.M., Liu, B., Hou, L., Yin, Y.T., Kang, Y.Y., Shi, Y., et al. (2016). The structural basis of the dominant negative phenotype of the Galphai1beta1gamma2 G203A/A326S heterotrimer. Acta pharmacol. Sinica *37*, 1259–1272.

Liu, Q., Yang, D., Zhuang, Y., Croll, T.I., Cai, X., Dai, A., He, X., Duan, J., Yin, W., Ye, C., et al. (2021). Ligand recognition and G-protein coupling selectivity of cholecystokinin A receptor. Nat. Chem. Biol. *17*, 1238–1244.

Maeda, S., Koehl, A., Matile, H., Hu, H., Hilger, D., Schertler, G.F.X., Manglik, A., Skiniotis, G., Dawson, R.J.P., and Kobilka, B.K. (2018). Development of an antibody fragment that stabilizes GPCR/G-protein complexes. Nat. Commun. *9*, 3712.

Manglik, A. (2020). Molecular basis of opioid action: From structures to new leads. Biol. Psychiatry *87*, 6–14.

Manglik, A., Kruse, A.C., Kobilka, T.S., Thian, F.S., Mathiesen, J.M., Sunahara, R.K., Pardo, L., Weis, W.I., Kobilka, B.K., and Granier, S. (2012). Crystal structure of the micro-opioid receptor bound to a morphinan antagonist. Nature *485*, 321–326.

Manglik, A., Lin, H., Aryal, D.K., McCorvy, J.D., Dengler, D., Corder, G., Levit, A., Kling, R.C., Bernat, V., Hübner, H., et al. (2016). Structure-based discovery of opioid analgesics with reduced side effects. Nature *537*, 185–190.

Mastronarde, D.N. (2005). Automated electron microscope tomography using robust prediction of specimen movements. J. Struct. Biol. *152*, 36–51.

Mather, L.E. (1983). Clinical pharmacokinetics of fentanyl and its newer derivatives. Clin. Pharmacokinet. *8*, 422–446.

Matthes, H.W., Maldonado, R., Simonin, F., Valverde, O., Slowe, S., Kitchen, I., Befort, K., Dierich, A., Le Meur, M., Dollé, P., et al. (1996). Loss of morphine-induced analgesia, reward effect and withdrawal symptoms in mice lacking the mu-opioid-receptor gene. Nature *383*, 819–823.

Mattson, C.L., Tanz, L.J., Quinn, K., Kariisa, M., Patel, P., and Davis, N.L. (2021). Trends and geographic patterns in drug and synthetic opioid overdose deaths - United States, 2013–2019. MMWR Morb. Mortal. Wkly. Rep. *70*, 202–207.

McCorvy, J.D., Wacker, D., Wang, S., Agegnehu, B., Liu, J., Lansu, K., Tribo, A.R., Olsen, R.H.J., Che, T., Jin, J., et al. (2018). Structural determinants of 5-HT2B receptor activation and biased agonism. Nat. Struct. Mol. Biol. *25*, 787–796.

Montandon, G., Ren, J., Victoria, N.C., Liu, H., Wickman, K., Greer, J.J., and Horner, R.L. (2016). G-protein-gated inwardly rectifying potassium channels modulate respiratory depression by opioids. Anesthesiology *124*, 641–650.

Pettersen, E.F., Goddard, T.D., Huang, C.C., Couch, G.S., Greenblatt, D.M., Meng, E.C., and Ferrin, T.E. (2004). UCSF Chimera–a visualization system for exploratory research and analysis. J. Comput. Chem. *25*, 1605–1612.

Pettersen, E.F., Goddard, T.D., Huang, C.C., Meng, E.C., Couch, G.S., Croll, T.I., Morris, J.H., and Ferrin, T.E. (2021). UCSF ChimeraX: structure visualization for researchers, educators, and developers. Protein Sci. *30*, 70–82.

Raehal, K.M., Walker, J.K., and Bohn, L.M. (2005). Morphine side effects in beta-arrestin 2 knockout mice. J. Pharmacol. Exp. Ther. *314*, 1195–1201.

Rasmussen, S.G., DeVree, B.T., Zou, Y., Kruse, A.C., Chung, K.Y., Kobilka, T.S., Thian, F.S., Chae, P.S., Pardon, E., Calinski, D., et al. (2011). Crystal structure of the beta2 adrenergic receptor-Gs protein complex. Nature *477*, 549–555.

Ricarte, A., Dalton, J.A.R., and Giraldo, J. (2021). Structural assessment of agonist efficacy in the mu-opioid receptor: morphine and fentanyl elicit different activation patterns. J. Chem. Inf. Model. *61*, 1251–1274.

Ringuette, A.E., Spock, M., Lindsley, C.W., and Bender, A.M. (2020). DARK classics in chemical neuroscience: carfentanil. ACS Chem. Neurosci. *11*, 3955–3967.

Roe, D.R., and Cheatham, T.E., 3rd. (2013). PTRAJ and CPPTRAJ: software for processing and analysis of Molecular Dynamics trajectory data. J. Chem. Theor. Comput. *9*, 3084–3095.

Rohou, A., and Grigorieff, N. (2015). CTFFIND4: fast and accurate defocus estimation from electron micrographs. J. Struct. Biol. *192*, 216–221.

Sanchez-Garcia, R., Gomez-Blanco, J., Cuervo, A., Carazo, J.M., Sorzano, C.O.S., and Vargas, J. (2021). DeepEMhancer: a deep learning solution for cryo-EM volume post-processing. Commun. Biol. *4*, 874.

Schmid, C.L., Kennedy, N.M., Ross, N.C., Lovell, K.M., Yue, Z., Morgenweck, J., Cameron, M.D., Bannister, T.D., and Bohn, L.M. (2017). Bias factor and therapeutic window correlate to predict safer opioid analgesics. Cell *171*, 1165–1175.e13.

Schmidtke, P., Bidon-Chanal, A., Luque, F.J., and Barril, X. (2011). MDpocket: open-source cavity detection and characterization on molecular dynamics trajectories. Bioinformatics *27*, 3276–3285.

Shao, Z., Shen, Q., Yao, B., Mao, C., Chen, L.N., Zhang, H., Shen, D.D., Zhang, C., Li, W., Du, X., et al. (2022). Identification and mechanism of G protein-biased ligands for chemokine receptor CCR1. Nat. Chem. Biol. *18*, 264–271.

Singla, N.K., Skobieranda, F., Soergel, D.G., Salamea, M., Burt, D.A., Demitrack, M.A., and Viscusi, E.R. (2019). APOLLO-2: A randomized, placebo and active-controlled Phase III study investigating oliceridine (TRV130), a G protein-biased ligand at the mu-opioid receptor, for management of moderate to severe acute pain following abdominoplasty. Pain Pract. *19*, 715–731.

Staus, D.P., Hu, H., Robertson, M.J., Kleinhenz, A.L.W., Wingler, L.M., Capel, W.D., Latorraca, N.R., Lefkowitz, R.J., and Skiniotis, G. (2020). Structure of the M2 muscarinic receptor-beta-arrestin complex in a lipid nanodisc. Nature *579*, 297–302.

Swanson, D.M., Hair, L.S., Strauch Rivers, S.R., Smyth, B.C., Brogan, S.C., Ventoso, A.D., Vaccaro, S.L., and Pearson, J.M. (2017). Fatalities involving carfentanil and furanyl fentanyl: two case reports. J. Anal. Toxicol. *41*, 498–502.

Thompson, A.A., Liu, W., Chun, E., Katritch, V., Wu, H., Vardy, E., Huang, X.P., Trapella, C., Guerrini, R., Calo, G., et al. (2012). Structure of the nociceptin/orphanin FQ receptor in complex with a peptide mimetic. Nature *485*, 395–399.

Tian, C., Kasavajhala, K., Belfon, K.A.A., Raguette, L., Huang, H., Migues, A.N., Bickel, J., Wang, Y., Pincay, J., Wu, Q., et al. (2020). ff19SB: amino-acid-specific protein backbone parameters trained against quantum mechanics energy surfaces in solution. J. Chem. Theor. Comput. *16*, 528–552.

Vass, M., Podlewska, S., de Esch, I.J.P., Bojarski, A.J., Leurs, R., Kooistra, A.J., and de Graaf, C. (2019). Aminergic GPCR-ligand interactions: A chemical and structural map of receptor mutation data. J. Med. Chem. *62*, 3784–3839.

Viscusi, E.R., Skobieranda, F., Soergel, D.G., Cook, E., Burt, D.A., and Singla, N. (2019). APOLLO-1: a randomized placebo and active-controlled phase III study investigating oliceridine (TRV130), a G protein-biased ligand at the micro-opioid receptor, for management of moderate-to-severe acute pain following bunionectomy. J. Pain Res. *12*, 927–943.

Vo, Q.N., Mahinthichaichan, P., Shen, J., and Ellis, C.R. (2021). How mu-opioid receptor recognizes fentanyl. Nat. Commun. *12*, 984.

Waldhoer, M., Bartlett, S.E., and Whistler, J.L. (2004). Opioid receptors. Annu. Rev. Biochem. *73*, 953–990.

Wang, H., Hetzer, F., Huang, W., Qu, Q., Meyerowitz, J., Kaindl, J., Hübner, H., Skiniotis, G., Kobilka, B.K., and Gmeiner, P. (2022). Structure-based evolution of G protein-biased mu-opioid receptor agonists. Angew. Chem. Int. Ed. Engl. *61*, e202200269.

Weiser, J., Shenkin, P.S., and Still, W.C. (1999). Approximate atomic surfaces from linear combinations of pairwise overlaps (LCPO). J. Comput. Chem. *20*, 217–230.

Wingler, L.M., Elgeti, M., Hilger, D., Latorraca, N.R., Lerch, M.T., Staus, D.P., Dror, R.O., Kobilka, B.K., Hubbell, W.L., and Lefkowitz, R.J. (2019). Angiotensin analogs with divergent bias stabilize distinct receptor conformations. Cell *176*, 468–478.e11.

Wu, E.L., Cheng, X., Jo, S., Rui, H., Song, K.C., Dávila-Contreras, E.M., Qi, Y., Lee, J., Monje-Galvan, V., Venable, R.M., et al. (2014). CHARMM-GUI Membrane Builder toward realistic biological membrane simulations. J. Comput. Chem. *35*, 1997–2004.

Xu, P., Huang, S., Zhang, H., Mao, C., Zhou, X.E., Cheng, X., Simon, I.A., Shen, D.D., Yen, H.Y., Robinson, C.V., et al. (2021). Structural insights into the lipid and ligand regulation of serotonin receptors. Nature *592*, 469–473.

Xu, Z., Ikuta, T., Kawakami, K., Kise, R., Qian, Y., Xia, R., Sun, M.X., Zhang, A., Guo, C., Cai, X.H., et al. (2022). Structural basis of sphingosine-1-phosphate receptor 1 activation and biased agonism. Nat. Chem. Biol. *18*, 281–288.

Zhang, K. (2016). Gctf: real-time CTF determination and correction. J. Struct. Biol. *193*, 1–12.

Zheng, S.Q., Palovcak, E., Armache, J.P., Verba, K.A., Cheng, Y., and Agard, D.A. (2017). MotionCor2: anisotropic correction of beam-induced motion for improved cryo-electron microscopy. Nat. Methods *14*, 331–332.

Zhuang, Y., Liu, H., Edward Zhou, X., Kumar Verma, R., de Waal, P.W., Jang, W., Xu, T.H., Wang, L., Meng, X., Zhao, G., et al. (2020). Structure of formylpeptide receptor 2-Gi complex reveals insights into ligand recognition and signaling. Nat. Commun. *11*, 885.

Zhuang, Y., Xu, P., Mao, C., Wang, L., Krumm, B., Zhou, X.E., Huang, S., Liu, H., Cheng, X., Huang, X.P., et al. (2021). Structural insights into the human D1 and D2 dopamine receptor signaling complexes. Cell *184*, 931–942.e18.

Zivanov, J., Nakane, T., Forsberg, B.O., Kimanius, D., Hagen, W.J., Lindahl, E., and Scheres, S.H. (2018). New tools for automated high-resolution cryo-EM structure determination in RELION-3. eLife *7*, e42166.

STAR★METHODS

KEY RESOURCES TABLE

REAGENT or RESOURCE	SOURCE	IDENTIFIER
Antibodies		
GP64-PE antibody	Expression systems	Cat# 97-201, RRID; AB_2922960
Anti-HA-FITC antibody, Mouse monoclonal	Sigma-Aldrich	Cat# H7411, RRID; AB_439704
Chemicals, Peptides, and Recombinant Proteins		
Fentanyl	Yuansi Technology	Cat# FN-0001
Morphine	Shenyang First Pharmaceutical	N/A
[D-Ala^2, *N*-MePhe^4, Gly-ol]-enkephalin (DAMGO)	Med Chem Express	Cat# HY-P0210B
PZM21	Med Chem Express	Cat# HY-101386
Oliceridine hydrochloride (TRV130)	TargetMol, USA	Cat# T13236L
SR17018	TargetMol, USA	Cat# T4407
Carfentanil	Yuansi Technology	Cat# FN-0170
Remifentanil	Yuansi Technology	Cat# FN-0159
Sufentanil	Yuansi Technology	Cat# FN-0160
Ohmefentanyl	Yuansi Technology	Cat# FN-0155
FBD1	This paper	N/A
FBD3	This paper	N/A
Lauryl maltose neopentyl glycol	Anatrace	Cat# NG310
Glyco-diosgenin (GDN)	Anatrace	Cat# GDN101
Cholesteryl Hemisuccinate	Anatrace	Cat# CH210
ClonExpress II One Step Cloning Kit	Vazyme Biotech	Cat# C112
PrimeSTAR Max Premix	TAKARA	R045Q
Protease Inhibitor Cocktail, EDTA-free	Bimake	Cat# B14003
Apyrase	New England Biolabs	Cat# M0398L
Tris-(2-carboxyethyl)-phosphine hydrochloride (TCEP)	Sangon Biotech	Cat# A600974
Nickel Sepharose resin	GE healthcare	Cat# 17526801
Anti-Flag resin	Smart-Lifesciences	Cat# C20042002
FLAG peptide	Genscript	Custom Synthesis
ESF921 culture medium	Expression systems	Cat# 96-001-01
Amylose resin	Smart-Lifesciences	Cat# SA026500
Dulbecco's Modified Eagle Medium (DMEM)	Gibco	Cat# 12800-017
Fetal Bovine Serum (FBS)	Gibco	Cat# 10099-141
Hanks' Balanced Salt Solution (HBSS)	Invitrogen	Cat# 14065-056
Critical Commercial Assays		
Bac-to-Bac Baculovirus Expression System	ThermoFisher	Cat# 10359016
Nano-Glo live Cell Assay System	Promega	Cat# N2013
LANCE UltracAMP kit	Perkinelmer	Cat# 2952744
Deposited Data		
μOR-fentanyl-G_i-scFv16 coordinate	This paper	PDB: 8EF5
μOR-morphine-G_i-scFv16 coordinate	This paper	PDB: 8EF6
μOR-DAMGO-G_i coordinate	This paper	PDB: 8EFQ
μOR-TRV130-G_i-scFv16 coordinate	This paper	PDB: 8EFB
μOR-PZM21-G_i-scFv16 coordinate	This paper	PDB: 8EFO
μOR-SR17018-G_i-scFv16 coordinate	This paper	PDB: 8EFL
μOR-fentanyl-G_i-scFv16 EM map	This paper	EMDB: EMD-28066

(*Continued on next page*)

Continued

REAGENT or RESOURCE	SOURCE	IDENTIFIER
μOR-morphine-G_i-scFv16 EM map	This paper	EMDB: EMD-28069
μOR-DAMGO-G_i EM map	This paper	EMDB: EMD-28088
μOR-TRV130-G_i-scFv16 EM map	This paper	EMDB: EMD-28077
μOR-SR17018-G_i-scFv16 EM map	This paper	EMDB: EMD-28085
μOR-PZM21-G_i-scFv16 EM map	This paper	EMDB: EMD-28086
μOR-DAMGO-G_i-scFv16	Koehl et al., 2018	PDB: 6DDE
μOR-DAMGO-G_i	Koehl et al., 2018	PDB: 6DDF
M_2R-β-arrestin1	Staus et al., 2020	PDB: 6U1N
NTSR1-β-arrestin1	Huang et al., 2020	PDB: 6UP7
δOR-DPI-287	Claff et al., 2019	PDB: 6PT3
κOR-MP1104	Che et al., 2018	PDB: 6B73
μOR-β-FNA	Manglik et al., 2012	PDB: 4DKL
μOR-BU72	Huang et al., 2015	PDB: 5C1M
CCK1R-CCK8-G_i-scFv16 EM map	Liu et al., 2021	EMDB: EMD-31387
Experimental Models: Organisms/strains		
E. coli strain BL21 (DE3)	NEB	Cat# C2527
TOP10 Competent *E. coli*	TIANGEN Biotech	Cat# CB104
Experimental Models: Cell Lines		
Spodoptera frugiperda Sf9 cells	Expression Systems	Cat# 94-001F
HEK293 cells	ATCC	Cat# CRL-1573
Recombinant DNA		
pFastbac-prolactin-FLAG-tev-μOR(1-388)-His8	This paper	N/A
pFastbac-HA-μOR(1-368)-LgBiT-tev-oMBP-MBP-His8	This paper	N/A
pFastbac-HA-μOR(1-368, F158W)-LgBiT-tev-oMBP-MBP-His8	This paper	N/A
pFastbac-$G_{\alpha i1}$2M (G203A, A326A)	This paper	N/A
pFastbac-H8-$G_{\beta 1}$	This paper	N/A
pFastbac-$G_{\gamma 2}$	This paper	N/A
pFastbac-GP67-scFv16-Tev-His8	This paper	N/A
pcDNA3.1-HA-μOR-SmBit	This paper	N/A
pBit1.1-LgBit-β-arrestin 2	This paper	N/A
pBit1.1-LgBit-β-arrestin 1	This paper	N/A
pcDNA3.1-myc-LgBit-miniG_{i1}	This paper	N/A
pcDNA3.1-myc-LgBit-miniG_o	This paper	N/A
Software and Algorithms		
Clonemanager	Sci-Ed Software	http://www.scied.com/pr_cmpro.htm
Prism 8	GraphPad	https://www.graphpad.com/scientific-software/prism/
SerialEM	Mastronarde, 2005	http://bio3d.colorado.edu/SerialEM/
MotionCor2	Zheng et al., 2017	https://emcore.ucsf.edu/ucsf-software
Ctffind4	Rohou and Grigorieff, 2015	https://grigoriefflab.umassmed.edu/ctf_estimation_ctffind_ctftilt
GCTF v1.06	Zhang, 2016	https://www2.mrc-lmb.cam.ac.uk/download/gctf_v1-06-and-examples/
Relion 3.1	Zivanov et al., 2018	https://relion.readthedocs.io/en/release-3.1/Installation.html
ResMap	Kucukelbir et al., 2014	http://resmap.sourceforge.net/
UCSF Chimera	Pettersen et al., 2004	https://www.cgl.ucsf.edu/chimera/

(*Continued on next page*)

Continued

REAGENT or RESOURCE	SOURCE	IDENTIFIER
UCSF ChimeraX	Pettersen et al., 2021	https://www.cgl.ucsf.edu/chimerax/
DeepEMhancer	Sanchez-Garcia et al., 2021	https://github.com/rsanchezgarc/deepEMhancer
Phenix	Adams et al., 2010	https://www.phenix-online.org/
MolProbity	Chen et al., 2010	http://molprobity.biochem.duke.edu/
Coot	Emsley and Cowtan, 2004	https://www2.mrc-lmb.cam.ac.uk/personal/pemsley/coot/
PyMol software	Schrödinger	https://pymol.org/2/
Adobe Illustrator CC	Adobe	https://www.adobe.com
CPPTRAJ	Roe and Cheatham, 2013	https://ambermd.org/
MDpocket	Schmidtke et al., 2011	https://github.com/Discngine/fpocket
Maestro	Schrödinger	https://schrodinger.com/
CHARMM-GUI	Jo et al., 2017	https://charmm-gui.org/?doc=input/membrane.bilayer
Amber 20	Amber	https://ambermd.org/
Other		
100 kDa molecular weight cut-off	Amicon Ultra	Cat# UFC910024
Quantifoil R1.2/1.3 300-mesh gold grids	Quantifoil	https://www.emsdiasum.com/microscopy/products/grids/quantifoil.aspx
Superdex 200 10/300GL Increase column	GE healthcare	Cat# 28990944

RESOURCE AVAILABILITY

Lead contact

Further information and requests for reagents may be directed and will be fulfilled by the lead contact, H. Eric Xu (eric.xu@simm.ac.cn).

Materials availability

All stable reagents generated in this study are available from the lead contact without restriction. Plasmids and strains are available from the authors upon request.

Data and code availability

- The 3D cryo-EM density maps of fentanyl-, morphine-, DAMGO-, SR17018-, PZM21-, and TRV130- bound μOR-G_i-scFv16 structures have been deposited in the Electron Microscopy Data Bank (EMDB) under the accession numbers EMD-28066, EMD-28069, EMD-28088, EMD-28085, EMD-28086 and EMD-28077, respectively. Atomic coordinates for the atomic models of fentanyl-, morphine-, DAMGO-, SR17018-, PZM21-, and TRV130- bound μOR-G_i-scFv16 structures have been deposited in the Protein Data Bank (PDB) under the accession numbers 8EF5, 8EF6, 8EFQ, 8EFL, 8EFO and 8EFB, respectively. These accession numbers are also listed in the key resources table.
- This paper does not report original code.
- Any additional information required to reanalyze the data reported in this paper is available from the lead contact upon request.

EXPERIMENTAL MODEL AND SUBJECT DETAILS

Spodoptera frugiperda (Sf9, Expression systems) cells were used for recombinant protein expression while HEK293 cells (ATCC) were used for functional studies. The Sf9 cells were grown in ESF 921 medium (Expression systems) at 27°C, 120 rpm. HEK293 cells were grown in humidified 37°C incubator in condition of 5% CO_2. The medium for human cell lines HEK293 was DMEM High-Glucose (Gibco) containing 10% fetal bovine serum (FBS, Gibco).

METHOD DETAILS

Cloning design of μOR and G_i heterotrimer

The wild type (WT) human μOR was used for cryo-EM sample preparation of morphine, fentanyl, DAMGO, SR17018 and PZM21 bound μOR-G_i complexes, for TRV130 bound μOR-G_i complex, a commonly used point mutation $F^{3.41}W$ was induced to stabilize

the signaling complex (Heydenreich et al., 2015; Xu et al., 2021). For morphine, fentanyl, SR17018 and PZM21 bound μOR-G_i complexes, the nucleotide coding sequence of μOR (1-388) was fused with an N-terminal FLAG tag followed by a TEV cleavage site, and a C-terminal His8 tag for purification of protein complexes (Figure S1A). The prolactin precursor sequence was inserted onto the N terminus as signaling peptide to assist anchoring μOR to the Sf9 insect cell membrane and elevate receptor expression level. For DAMGO and TRV130 bound μOR-G_i complexes, we fused haemagglutinin (HA) signal peptide at the N-terminal of μOR (1-368), the C-terminus was followed by LgBiT with a TEV protease cleavage site and an oMBP-MBP tag to facilitate expression and purification (Figure S1A). The modified μOR sequences were all constructed into the pFastBac vector (ThermoFisher) for expression usage. Two dominant-negative mutations, G203A and A326S, were incorporated into the human $G_{\alpha i1}$ ($G_{\alpha i1}$_2M) by site direct mutagenesis to decrease the binding of GDP/GTP and increase the stability of G protein (Liu et al., 2016). In addition, a His8 tag was cloned to the N terminus of G_β for two-step purification strategy usage. As for the μOR construct fused with LgBit, the G_β fused with a His8 tag at N terminus as well as a 15 residues linker and the SmBiT tag at C terminus was used to link the LgBiT behind μOR in the later co-expression procedure (Duan et al., 2020; Figure S1A). All the three components of G_{i1} heterotrimer, human $G_{\alpha i1}$_2M, rat His8-G_β or His8-G_β-SmBiT and bovine G_γ, were constructed into the pFastBac vector (ThermoFisher), respectively.

Expression and purification of the μOR-G_i signaling complexes

The single chain antibody scFv16 was prepared in advance. For the expression of scFv16, the coding sequence of scFv16 was fused with a GP67 signaling peptide at the N terminus and a TEV cleavage site-His8 at the C terminus, and then cloned into the pFastBac vector (Thermo Fisher). Preparation of scFv16 stocks was conducted as previously described (Maeda et al., 2018; Zhuang et al., 2020).

The baculoviruses of μOR, $G_{\alpha i1}$_2M, $G_{\beta 1}$ and $G_{\gamma 2}$ were generated and amplified using the Bac-to-Bac baculovirus expression system (ThermoFisher). The Sf9 cells were cultured in ESF 921 serum-free medium (Expression Systems). The four types of baculoviruses expressing μOR, $G_{\alpha i1}$_2M, $G_{\beta 1}$ and $G_{\gamma 2}$ were co-expressed in Sf9 insect cells (Invitrogen) at the ratio of 1:1:1:1 when the cell density reached to 4 × 10^6 cells/mL. After incubation for 48 hours, the cells were collected by centrifugation at 2000 rpm (ThermoFisher, H12000) for 20 min and the cell precipitates were kept frozen at -80°C for further protein purification.

For the purification of μOR-G_i complexes, cell pellets from 1 liter culture were thawed at room temperature and resuspended in low salt buffer containing 20 mM HEPES pH 7.2, 50 mM NaCl, 10mM KCl, 5 mM $MgCl_2$, 0.3 mM TCEP, protease inhibitor cooktail (Bimake, 1 mL/ 100 mL suspension). The suspensions were treated with French Press and centrifugated at 100,000 × g for 30 min at 4°C. The cell precipitates after centrifugation were collected and resuspended in buffer containing 20 mM HEPES pH 7.2, 75 mM NaCl, 5 mM $CaCl_2$, 5 mM $MgCl_2$, 5% glycerol, 0.3 mM TCEP, protease inhibitor cooktail (Bimake, 1 mL/ 100 mL suspension). The μOR-G_i complexes were assembled on membrane by addition of synthesized compound ligands 10 μM morphine (Shenyang First Pharmaceutical Co., Ltd.), 10 μM fentanyl (Yuansi Technology Co., Ltd.), 20 μM SR17018 (TargetMol), 10 μM PZM21(Med Chem Express), 10 μM TRV130 (TargetMol) and peptide agonist 10 μM DAMGO (Med Chem Express), respectively. After incubating at room temperature for half an hour, the cell suspension was treated with apyrase (25 mU mL^{-1}, NEB), followed by incubation for another 1 hour at room temperature. Cell membranes in suspension was solubilized directly by adding 0.5% (w/v) lauryl maltose neopentylglycol (LMNG, Anatrace), 0.1% (w/v) cholesteryl hemisuccinate TRIS salt (CHS, Anatrace). After membrane solubilization for 3 hours at 4°C, the solubilized fractions were isolated by centrifugation at 100,000 × g for 45 min and then incubated overnight at 4°C with pre-equilibrated Nickel-NTA resin (4 mL resin/1 L cell culture). After batch binding, the nickel resin with immobilized protein complex was manually loaded onto a gravity flow column. The nickel resin was washed with 10 column volumes of 20 mM HEPES, pH 7.2, 100 mM NaCl, 25 mM imidazole, 0.3 mM TCEP, 0.05% LMNG (w/v), 0.01% CHS (w/v), 5 μM ligands and eluted with the same buffer containing 300 mM imidazole.

For morphine, fentanyl, SR17018 and PZM21 bound μOR-G_i complexes, the Ni-NTA eluate was further incubated by batch binding with 2 mL FLAG resin (Smart-Lifesciences) for 2 hours at 4°C. The FLAG resin embedded with protein complexes was then washed by 10 column volumes of detergent buffer containing 20 mM HEPES, pH 7.2, 100 mM NaCl, 0.3 mM TCEP, 0.0075% LMNG (w/v), 0.0025% GDN, 0.002% CHS (w/v), 5 μM ligands. Subsequently, the material bound to FLAG resin was then eluted in the same detergent buffer containing 200 μg/μL FLAG peptide. For DAMGO and TRV130 bound μOR-G_i complexes, the first step Ni-NTA eluate was transferred to pre-equilibrated amylose resin (Smart-Lifesciences) and incubated for 3 hours at 4°C. After batch binding, the amylose resin was washed with 10 column volumes of detergent buffer containing 20 mM HEPES, pH 7.2, 100 mM NaCl, 0.3 mM TCEP, 0.0075% LMNG (w/v), 0.0025% GDN, 0.002% CHS (w/v), 5 μM ligands. The amylose resin with bound material was then suspended and treated with TEV protease (homemade) and 2mg scFv16 for 1 h at room temperature, the released protein in the flowthrough was then collected.

The eluted or released protein sample was concentrated to 0.5 mL using centrifugal filter units with a molecular weight cutoff at 100 KDa (Millipore, Sigma) and loaded onto a Superdex 200 Increase 10/300 GL column (GE Healthcare) or Superose 6 Increase 10/300 GL column (GE Healthcare) pre-equilibrated with buffer containing 20 mM HEPES, pH 7.2, 100 mM NaCl, 0.00075% LMNG (w/v), 0.00025% GDN, 0.0002% CHS (w/v), 0.3 mM TCEP and 5 μM ligands. Fractions of main peak were collected and concentrated using 100 KDa centrifugal filter units (Millipore, Sigma) for the later electron microscopy experiments (Figures S1E–S1J).

Negative staining analysis

When we purified the SR17018-μOR-G_i-scFv16 complex sample by size exclusion chromatography, the retention volume of the protein complex indicated it to be dimer. The peak fraction of SR17018-μOR-G_i-scFv16 complex was then subjected to negative staining analysis to check the dimeric state. 5 μL protein samples at concentration of 10ng/ μL were applied to glow-discharged carbon coated copper grids. After waiting for 60 s, the grids were blotted by filter paper. Subsequently, 5 μL of 1% uranyl formate was applied to the grid and blotted immediately. Then, another 5 μL of 1% uranyl formate was added to the grid and the protein sample was stained for 60 s. Data were acquired using a Tecnai Spirit transmission electron microscope operating at 120 kV.

Cryo-EM grid preparation and data acquisition

For cryo-EM grid preparation, 3.0 μL morphine, fentanyl, DAMGO, SR17018, PZM21 and TRV130 bound μOR-G_i-scFv16 complex at the concentration of 14.8 mg mL^{-1}, 12.5 mg mL^{-1}, 3.7 mg mL^{-1}, 8.1 mg mL^{-1}, 15.2 mg mL^{-1}, 9.8 mg mL^{-1} was applied individually to EM grids (Quantifoil, 300 mesh Au R1.2/1.3) that were glow-discharged for 50s in a Vitrobot chamber (FEI Vitrobot Mark IV). Protein concentration was determined by absorbance at 280 nm using a Nanodrop 2000 Spectrophotometer (Thermo Fisher Scientific). Vitrification was performed at 100% humidity and 4°C. The sample was blotted for 3s before plunge-freezing into liquid ethane. The prepared cryo-EM grids were stored in liquid nitrogen for screening and data collection usage.

Before data collection, grids were previously screened with a FEI 200 kV Arctica transmission electron microscope (TEM), the promising grids with evenly distributed particles and thin ice layer were transferred to a FEI 300 kV Titan Krios TEM for further data collection.

For the morphine, fentanyl, SR17018 and TRV130 bound μOR-G_i-scFv16 complexes, automatic cryo-EM movie stacks were collected on a FEI Titan Krios microscope operated at 300kV accelerating voltage in Cryo-Electron Microscopy Research Center, Shanghai Institute of Materia Medica, Chinese Academy of Sciences (Shanghai, China). The microscope was operated with a nominal magnification of 81,000× in super-resolution counting mode, corresponding to a pixel size of 0.5355 Å. A total of 5,138 movies for the dataset of morphine-μOR-G_i-scFv16 complex, 4,375 movies for the dataset of fentanyl-μOR-G_i-scFv16 complex, 4,436 movies for the dataset of SR17018-μOR-G_i-scFv16 complex and 3,523 movies for the dataset of TRV130-μOR-G_i-scFv16 complex were collected individually by a Gatan K3 Summit direct electron detector equipped with a Gatan energy filter (operated with a slit width of 20 eV) (GIF) using the SerialEM software (Mastronarde, 2005). The images were recorded at a dose rate of about 23.3 e/$Å^2$/s with a defocus ranging from -0.5 to -3.0 μm. The total exposure time was 3 s and intermediate frames were recorded in 0.083 s intervals, resulting in a total of 36 frames per micrograph.

For the DAMGO bound μOR-G_i-scFv16 complexes, automatic cryo-EM movie stacks were collected on a FEI Titan Krios microscope operated at 300kV accelerating voltage in Cryo-Electron Microscopy Research Center, Shanghai Institute of Materia Medica, Chinese Academy of Sciences (Shanghai, China). The microscope was operated at 300 kV accelerating voltage, at a nominal magnification of 46,685× in counting mode, corresponding to a pixel size of 1.071 Å. A total of 4,753 movies were obtained with a defocus range of -1.2 to -2.2 μm. An accumulated dose of 70 electrons per $Å^2$ was fractionated into a movie stack of 36 frames.

For the PZM21-μOR-G_i-scFv16 complex, automatic cryo-EM movie stacks were collected on a FEI Titan Krios microscope operated at 300kV in Advanced Center for Electron Microscopy, Shanghai Institute of Materia Medica, Chinese Academy of Sciences (Shanghai, China). The microscope was equipped with a Gatan Quantum energy filter. The movie stacks were collected automatically using a Gatan K3 direct electron detector with a nominal magnification of 105,000× in super-resolution counting mode at pixel size of 0.412 Å. The energy filter was operated with a slit width of 20 eV. Each movie stack was dose-fractionated in 36 frames with the dose of 1.39 electrons per frame and collected within a defocus ranging from -0.5 to -3.0 μm. The total exposure time was 2.35 s. A total of 5,942 movies were collected. Data collection was performed using EPU with one exposure per hole on the grid squares.

Image processing and 3D reconstruction

Movie stacks were subjected to beam-induced motion correction using MotionCor 2.1 (Zheng et al., 2017). For the datasets of morphine, fentanyl, SR17018 and TRV130 bound μOR-G_i-scFv16 complexes, movie stack was aligned, dose weighted and binned by 2 to 1.071 Å per pixel. For the datasets of PZM21-μOR-G_i-scFv16 complex, movie stacks were aligned, dose weighted and binned by 2 to 0.824 Å per pixel. Data processing was performed using RELION-3.1 (Zivanov et al., 2018). Contrast transfer function (CTF) parameters were estimated by Ctffind4 (Rohou and Grigorieff, 2015).

For the SR17018-μOR-G_i-scFv16 complex, the micrographs with resolution worse than 4.0 Å and micrographs imaged within the carbon area of grid squares were abandoned, producing 4,308 micrographs to do further data processing. About 2000 particles were manually selected and subjected to 2D classification. Representative averages were chosen as template for particle auto-picking. The auto-picking process produced 4,496,715 particles, which were subjected to reference-free 2D classifications to discard bad particles. Initial reference map models for 3D classification were generated by RELION using the representative 2D averages. The particles selected from 2D classification were subjected to 3D classifications. The first two rounds 3D classification results further indicated that the SR17018-μOR-G_i-scFv16 complex existed as anti-parallel dimer, in which only one of the G protein heterotrimers showed clear density. Another 5 rounds 3D classifications were performed with a mask excluding the G protein heterotrimer with poor density. The 3D classifications resulting in a single well-defined subset with 355,281 particles. Further 3D refinement, CTF refinement and Bayesian polishing generated a density map with an indicated global resolution of 3.2 Å at a Fourier shell correlation of 0.143.

For the morphine, fentanyl, PZM21 and TRV130 bound μOR-G_i-scFv16 complexes, the micrographs with resolution worse than 4.0 Å and micrographs imaged within the carbon area of grid squares were abandoned, producing 4,197 micrographs, 4,319 micrographs, 5,661 micrographs, 2,769 micrographs, respectively, to do further data processing. The 3D density map of SR17018-μOR-G_i-scFv16 complex dimer low-pass filtered to 40 Å was chosen as reference map for auto-picking and further 3D classification processes for morphine, fentanyl and PZM21 bound μOR-G_i-scFv16 datasets, while the 3D density map of CCK1R-CCK8-G_i (EMDB ID EMD-31387) (Liu et al., 2021) low-pass filtered to 40 Å was chosen as reference map for auto-picking and further 3D classification for TRV130-μOR-G_i-scFv16 dataset. The 2D and 3D classifications were performed on a binned dataset with a pixel size of 2.142 Å. The auto-picking process produced 5,125,620 particles for morphine-μOR-G_i-scFv16 complex, 4,197,617 particles for fentanyl-μOR-G_i-scFv16 complex, 5,674,868 particles for PZM21-μOR-G_i-scFv16 complex and 2,256,278 particles for TRV130-μOR-G_i-scFv16 complex, which were subjected to reference-free 2D classifications to discard bad particles. Particles selected from 2D classification were then subjected to several rounds 3D classifications. Similar anti- parallel dimer conformations as SR17018-μOR-G_i-scFv16 complex were observed in morphine, fentanyl and PZM21 bound μOR-G_i-scFv16 datasets, while the TRV130-μOR-G_i-scFv16 complex existed as stable monomer. As to morphine, fentanyl and PZM21 bound μOR-G_i-scFv16 particles, 3D classifications were performed with a mask excluding one of the G protein heterotrimers with poor density. The final 3D classifications lead to a single well-defined subset with 382,346 particles for morphine-μOR-G_i-scFv16 complex, a single well-defined subset with 291,861 particles for fentanyl-μOR-G_i-scFv16 complex and two well-defined subsets with 150,254 particles for PZM21-μOR-G_i-scFv16 complex. As for TRV130-μOR-G_i-scFv16 complex. The final 3D classifications lead to a single well-defined subset with 300,448 particles. Further 3D refinement, CTF refinement and Bayesian polishing generated a density map with indicated global resolutions of 3.2 Å, 3.3 Å, 2.8 Å and 3.2 Å for morphine, fentanyl, PZM21 and TRV130 bound μOR-G_i-scFv16 complexes, respectively. The resolutions were estimated by applying a soft mask around the protein densities with the FSC 0.143 criteria. A map generated by 3D refinement was subsequent post-processed in DeepEMhancer (Sanchez-Garcia et al., 2021) for fentanyl-μOR-G_i-scFv16 complex.

For DAMGO-μOR-G_i-scFv16 complex, dose-fractionated image stacks were subjected to beam-induced motion correction using MotionCor2.1 (Zheng et al., 2017). A sum of all frames, filtered according to the exposure dose, in each image stack was used for further processing. Contrast transfer function parameters for each micrograph were determined by Gctf v1.06 (Zhang, 2016). Particle selection, 2D and 3D classifications were performed on a binned dataset with a pixel size of 2.142 Å using RELION-3.1.1 (Zivanov et al., 2018). Auto-picking yielded 3,984,244 particle projections that were subjected to reference-free 2D classification to discard false positive particles or particles categorized in poorly defined classes, producing 1,729,374 particle projections for further processing. This subset of particle projections was subjected to a round of maximum-likelihood-based 3D classifications with a pixel size of 2.142 Å, resulting in one well-defined subset. Further 3D classifications with mask on the complex produced one good subset of 602,466 particles, which were subjected to another round of 3D classifications with mask on the receptor. A selected subset containing 305,004 projections was then subjected to 3D refinement and Bayesian polishing with a pixel size of 1.071 Å. After the last round of refinement, the final map has an indicated global resolution of 3.3 Å at a Fourier shell correlation (FSC) of 0.143.

Local resolution map was calculated using ResMap (Kucukelbir et al., 2014). Surface coloring of the density map was performed using UCSF Chimera (Pettersen et al., 2004). The data processing maps were generated using UCSF Chimera (Pettersen et al., 2004) and ChimeraX (Pettersen et al., 2021). In all the solved μOR-G_i complexes, no clear densities were observed in the N-terminal and C-terminal tails of μOR, which was similar to most reported GPCR-G protein complexes. Interestingly, several putative lipids densities were found surrounding the μOR-G_i homodimer packing interface of μOR, which may play important role in stabilizing the conformation of the interaction interface.

Model building, structure refinement, and figure preparation

The cryo-EM structure of mouse DAMGO-μOR-G_i complex (PDB code: 6DDE) was used as initial model for model rebuilding and refinement against the EM density map. The model was first fitted as a rigid body into the cryo-EM density maps using Chimera (Pettersen et al., 2004). Then, the models were refined in Phenix (Adams et al., 2010) and manually adjusted and rebuilt in Coot (Emsley and Cowtan, 2004). All ligands were created using ChemSketch (ACD/ChemSketch, version 2018.2.1, Advanced Chemistry Development, Inc., Toronto, ON, Canada, www.acdlabs.com, 2018), and manually adjusted based on electron density maps in Coot and refined together with the protein complexes in Phenix. The final complex models were validated by Molprobity (Chen et al., 2010). Cryo-EM data collection, image processing and structure refinement statistics are listed in the Table S2. Figures showing structural models and detailed structural information were prepared by PyMol 2.4.2 (https://pymol.org/2/). The maximum distance cutoffs for polar interactions and hydrophobic interactions were set at 3.5-Å and 4.5-Å, respectively.

Surface expression analysis

Cell-surface expression for WT μOR and mutants was monitored by a fluorescence-activated cell sorting (FACS) assay. In brief, HEK293 cells expressing HA-tagged μOR were harvested twenty-four hours after transfection. Cells were incubated with mouse anti-HA-FITC antibody (Sigma) at a dilution of 1:200 for 20 min at 4°C, and then a 9-fold excess of PBS was added to cells. Finally, the surface expression of μOR was monitored by detecting the fluorescent intensity of FITC with Guava easyCyte 8HT. The FACS data were analyzed by Guava software 2.1.

cAMP accumulation assay

For detecting G_i signaling of μOR, HEK293 cells expressing WT or mutant μOR were harvested and resuspended in DMEM containing 500 μM IBMX at a density of 2 ×10^5 cells/mL. Cells were then plated onto 384-well assay plates at 1000 cells/ 5 μL/ well. Another 5 μL buffer containing 1 μM Forskolin and various concentrations of test compounds were added to the cells. After incubation at room temperature for 15 minutes, intracellular cAMP level was tested by a LANCE Ultra cAMP kit (PerkinElmer, TRF0264) and EnVision multiplate reader according to the manufacturer's instructions.

$G_{\alpha i/o}$ and β-arrestin 2 recruitment assay

The recruitment of $G_{\alpha i/o}$ / β-arrestin 2 to μOR was measured using the Promega NanoBiT Protein-Protein Interaction System. In brief, HEK293 cells were cotransfected with plasmids encoding LgBiT-miniG_α/ LgBiT-β arrestin 2 and μOR -SmBiT at the ratio of 1:1. Twenty-four hours later, cells were harvested and resuspended in phenol red-free DMEM at a density of 1.2 ×10^6 cells/mL. After cells were plated onto 384-well assay plates at 12,000 cells/ 10 μL/ well, 10 μL/ well of Nano-Glo Live Cell reagent according to the manufacturer's protocol (Promega, Cat No: N2011) was added and incubated for 10 min at room temperature. Another 10 μL culture medium with various concentrations of compounds were added to the cells. After incubation at room temperature for 15 minutes, bioluminescence was measured with an EnVision multiplate reader (PerkinElmer).

Synthesis of FBD1 and FBD3

1-(4-fluorophenethyl)-3-methylpiperidin-4-one (1)

Cs_2CO_3 (17.3 g, 53.02 mmol) was added to a yellow solution of 3-methylpiperidin-4-one (3 g, 26.51 mmol), 1-(2-bromoethyl)-4-fluorobenzene (5.38 g, 26.51 mmol) and acetonitrile (100 mL). The reaction mixture was stirred at 80°C for 5 hrs. The reaction mixture was cooled to room temperature, diluted with water and extracted by ethyl acetate. The crude product was purified by silica gel column to give compound 1, which was a yellow oil. ^{1}H NMR (400 MHz, Chloroform-*d*) δ 7.18 (dd, *J* = 8.2, 5.4 Hz, 2H), 6.99 (t, *J* = 8.5 Hz, 2H), 3.19 (p, *J* = 5.9, 5.4 Hz, 2H), 2.82 (dd, *J* = 9.7, 6.2 Hz, 2H), 2.73 - 2.56 (m, 4H), 2.42 (ddt, *J* = 31.4, 13.9, 3.1 Hz, 2H), 2.16 (t, *J* = 11.1 Hz, 1H), 1.03 (d, *J* = 6.7 Hz, 3H).

1-(4-fluorophenethyl)-N-isopropyl-3-methylpiperidin-4-amine (2)

The compound 1 (500 mg, 2.12 mmol) and isopropylamine (125.6 mg, 2.12 mmol) were dissolved dichloromethane (10 mL) and AcOH (0.125 mL, 2.12 mmol) was added dropwise. Then the $NaBH(OAc)_3$ (675.3 mg, 3.19 mmol) was added to the yellow solution at ice bath. The reaction mixture was stirred at room temperature for overnight. The reaction mixture was diluted with water, extracted by dichloromethane, washed with brine and dried over Na_2SO_4. The crude product was purified by silica gel column to give compound 2, which was a white solid. ^{1}H NMR (400 MHz, Chloroform-*d*) δ 7.16 (dd, *J* = 8.3, 5.4 Hz, 2H), 6.96 (t, *J* = 8.5 Hz, 2H), 3.10 – 3.01 (m, 1H), 2.80 (dtd, *J* = 32.7, 25.0, 23.9, 8.3 Hz, 5H), 2.55 (qd, *J* = 12.1, 5.7 Hz, 2H), 2.37 - 2.00 (m, 3H), 1.92 - 1.75 (m, 2H), 1.25 (d, *J* = 6.5 Hz, 3H), 1.19 (d, *J* = 6.3 Hz, 3H), 1.08 (d, *J* = 6.9 Hz, 3H).

1-(4-fluorophenethyl)-3-methyl-N-propylpiperidin-4-amine (3)

The compound 1 (500 mg, 2.12 mmol) and propylamine (125.6 mg, 2.12 mmol) were dissolved dichloromethane (10 mL) and AcOH (0.125 mL, 2.12 mmol) was added dropwise. Then the $NaBH(OAc)_3$ (675.3 mg, 3.19 mmol) was added to the yellow solution at ice bath. The reaction mixture was stirred at room temperature for overnight. The reaction mixture was diluted with water, extracted by dichloromethane, washed with brine and dried over Na_2SO_4. The crude product was purified by silica gel column to give compound 3, which was a white solid. ^{1}H NMR (400 MHz, Chloroform-*d*) δ 7.17 (dd, *J* = 8.1, 5.5 Hz, 2H), 6.99 (q, *J* = 8.7 Hz, 2H), 2.85 - 2.51 (m, 8H), 2.30 (s, 2H), 2.14 (s, 1H), 1.59 (dh, *J* = 31.5, 7.4 Hz, 3H), 1.27 (s, 2H), 1.04 (dd, *J* = 15.0, 6.4 Hz, 3H), 0.96 (t, *J* = 7.3 Hz, 3H).

N-(1-(4-fluorophenethyl)-3-methylpiperidin-4-yl)-N-isopropylpropionamide (FBD1)

FBD1 was prepared from the intermediate compound 2 (210 mg, 0.754 mmol) and propionyl chloride (0.132 mL, 1.509 mmol). The residue was purified by silica gel column (dichloromethane/methyl alcohol, 10:1) to give product FBD1 as a orange solid (160 mg, yield: 63.42%). ^{1}H NMR (400 MHz, Chloroform-*d*) δ 7.20 (d, *J* = 6.9 Hz, 2H), 7.00 (t, *J* = 8.5 Hz, 2H), 4.11 (d, *J* = 9.6 Hz, 1H), 3.68 (d, *J* = 47.0 Hz, 2H), 3.28 (d, *J* = 92.3 Hz, 6H), 2.82 (s, 2H), 2.38 (p, *J* = 7.6 Hz, 2H), 2.04 (d, *J* = 13.7 Hz, 1H), 1.52 (d, *J* = 88.4 Hz, 1H), 1.29 - 0.85 (m, 12H); MS(ESI): m/z 335.4 (M + H) +.

N-(1-(4-fluorophenethyl)-3-methylpiperidin-4-yl)-N-propylpropionamide (FBD3)

FBD3 was prepared from the intermediate compound 3 (130 mg, 0.467 mmol) and propionyl chloride (0.082 mL, 0.934 mmol). The residue was purified by silica gel column (dichloromethane/methyl alcohol, 10:1) to give product FBD3 as a orange solid (92 mg, yield: 58.91%). ^{1}H NMR (400 MHz, Chloroform-*d*) δ 7.17 (dd, *J* = 8.2, 5.4 Hz, 2H), 6.97 (t, *J* = 8.5 Hz, 2H), 3.69 (q, *J* = 13.3, 12.3 Hz, 1H), 3.25 – 3.04 (m, 2H), 2.85 – 2.71 (m, 3H), 2.57 - 2.01 (m, 8H), 1.77 - 1.45 (m, 3H), 1.27 (s, 1H), 1.17 (t, *J* = 7.4 Hz, 3H), 1.06 (dd, *J* = 30.5, 7.1 Hz, 3H), 0.88 (dt, *J* = 12.1, 7.2 Hz, 3H). MS(ESI): m/z 335.4 (M + H) +.

Molecular docking analysis

The fentanyl-μOR complex was firstly prepared in Schrödinger, Maestro. In the preparation, hydrogens were added to systems with a pH of 7, and a restrained minimization process were then conducted to exclude conflicts. Based on the minimized structure, fentanyl derivatives, including carfentanil, lofentanil, ohmefentanyl, remifentanil and sufentanil, as well as the designed G protein-preferred fentanyl analogs FBD1 and FBD3, were docked to the corresponding pocket. In particular, the initial conformations of ligands

were generated by triangle matcher with London dG scoring. Next, refinement was employed with a rigid receptor under GBVI/WSA dG scoring to produce the output structure.

Molecular dynamics simulation

The ligand-bound complex structures of μOR were used to construct six molecular dynamics simulation systems including fentanyl, morphine, DAMGO, TRV130, PZM21 and SR17018, respectively. We used CHARMM-GUI server to insert complex structures to a palmitoyl-2-oleoyl-sn-glycero-3-phosphocholine (POPC) membrane, then solved with TIP3P water and 0.15 mol L^{-1} KCl to establish simulation systems (Jo et al., 2017; Lee et al., 2016; Wu et al., 2014). FF19SB, LIPID17, and GAFF2 force field was applied for the parameter of amino acids, lipids, and ligands, respectively (He et al., 2020; Lee et al., 2020a; Tian et al., 2020).

The following simulation processes were finished on Amber20. Firstly, the systems were minimized for solvents and then for all atoms. Next, all of them were heated to 300 K in 300 ps and equilibrated for 700 ps under NVT conditions with 10 kcal mol^{-1} $Å^{-2}$ restraint on proteins and lipids. Then, systems underwent 3×500 ns independent production runs under NPT condition with a time-step of 2 fs. During simulations, the temperature (300 K) and pressure (1 atm) were controlled by Langevin thermostat and Berendsen barostat, respectively. Long-range electrostatic interactions were treated by Particle mesh Ewald algorithm and a cutoff of 10 Å was employed for short-range electrostatic and van der Waals interactions. The SHAKE algorithm was applied to restrain the bond with hydrogens for covalent bonds containing hydrogen.

The analyses of simulation trajectories were finished by CPPTRAJ (Roe and Cheatham, 2013). In detail, to calculate the SASA, the residues within 5 Å of G protein in fentanyl-μOR-G protein structure were picked as G protein pocket residues. Then, their SASAs were calculated by 'surf' command in CPPTRAJ using the linear combination of pairwise overlaps method (LCPO) (Weiser et al., 1999). The pocket volumes were calculated by MDpocket (Schmidtke et al., 2011). In specific distance ranges (fentanyl and DAMGO: 6-8 Å, SR17018, TRV130, PZM21: 10-14 Å), the structure with the smallest C-alpha RMSD with other structures was extracted as the representative structure for the range via hieragglo algorithm, 'cluster' command in CPPTRAJ.

The contact profile was calculated by the 'nativecontacts' command in CPPTRAJ. For each snapshot in every system, the distance between every heavy atom in ligand and receptor was calculated. If the distance is smaller than 4 Å in one snapshot between an atom pair, the corresponding residue was determined to have contact with ligand in this snapshot. For the whole trajectories, if the residue has contacts with ligand in more than 40 % of all the time, the residue was marked as one with stable contacts and shown as sticks in Figure S6F.

Construction for μOR-β-arrestin1 model

M_2R-β-arrestin1 (PDB ID: 6U1N) and NTSR1-β-arrestin1 (PDB ID: 6UP7) were used for the construction of μOR-β-arrestin model 1 and model 2, respectively. During the process, M_2R and NTSR1 were firstly aligned to the representative structures. Then, μOR and β-arrestin structures were extracted from the complex for minimization with a 3.0 Å RMSD restraint on non-hydrogen atoms. The interface areas were calculated by averaging the SASA covered by β-arrestin in μOR and the SASA covered by μOR in β-arrestin.

Figure preparation

Structural figures were prepared in in UCSF Chimera (https://www.cgl.ucsf.edu/chimera/), Chimera X (https://www.cgl.ucsf.edu/chimerax/) and PyMOL (https://pymol.org/2/).

QUANTIFICATION AND STATISTICAL ANALYSIS

For cAMP accumulation assays and β-arrestin2 recruitment assays, results were analyzed using the sigmoidal log (agonist) versus dose response function built into GraphPad Prism software 8.0 (GraphPad Software Inc., San Diego, CA). Concentration-response curves were evaluated with a three-parameter logistic equation. The pEC_{50} and Span values were calculated for individual experiments using ''log (agonist) vs. response (three parameters)'' function in GraphPad Prism 8.0 software. Average E_{max} and basal values for assays were determined from the highest and lowest concentrations of the respective compound. The significance was determined with two-side, one-way ANOVA with Fisher's LSD test, and *$P < 0.05$; **$P < 0.01$, and ***$P < 0.001$ vs. wild-type (WT) was considered statistically significant. For surface expression levels of WT μOR and its mutants, values were normalized to wild-type receptor and graphed as a percentage of wild-type using GraphPad Prism 8.0. All the data in the figures and tables are presented as means ± SEM with the number of biological and technical replicates indicated in the figure and table legends.

CellPress

Supplemental figures

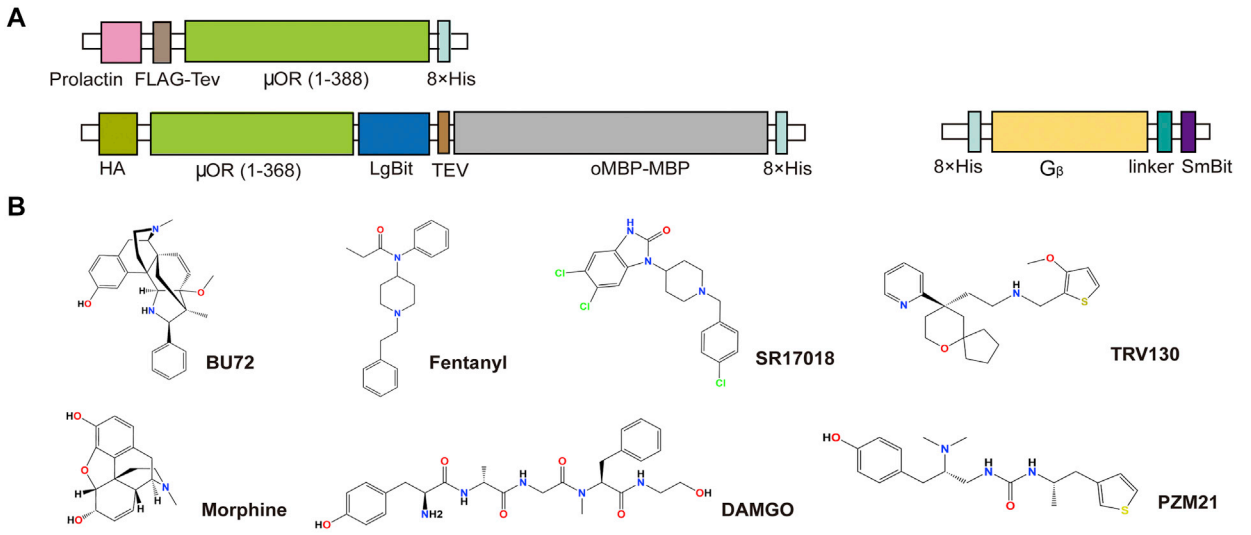

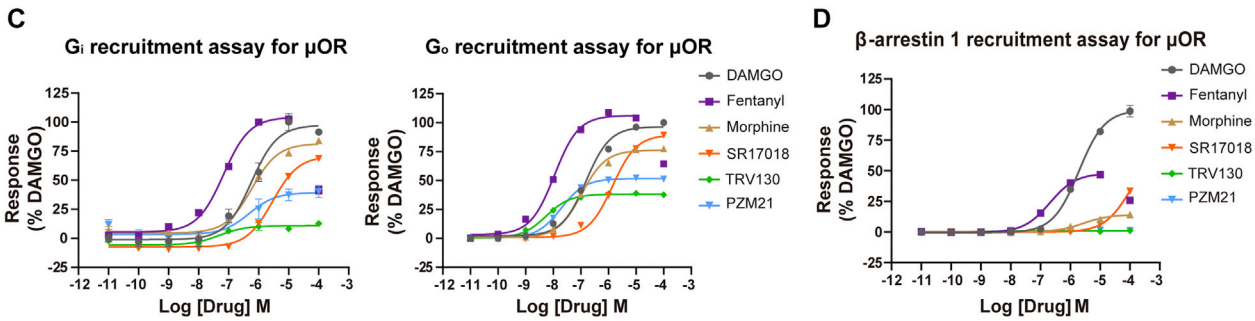

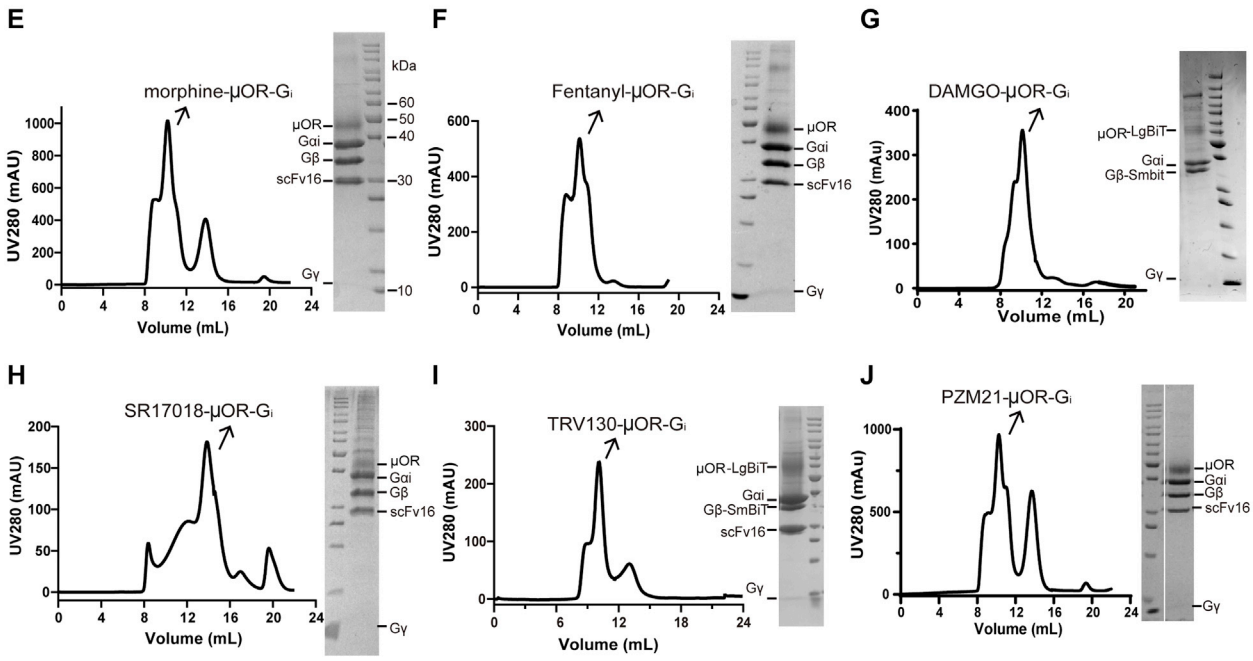

(legend on next page)

Figure S1. Construct design and protein preparation of μOR-G_i complexes, related to Figure 1

(A) Cartoon models of the μOR constructs and G_β-Smbit used in this study.

(B) Chemical structures of the six opiod agonists used (morphine, fentanyl, DAMGO, SR17018, TRV130, and PZM21).

(C and D) The signaling profiles of six opiod agonists, morphine, fentanyl, DAMGO, SR17018, TRV130, and PZM21, in G_i, G_o (C) and β-arrestin 1 recruitment (D) assays. DAMGO was used as the reference ligand. Data were presented as means ± SEM with a minimum of three technical replicates, which were performed in triplicates each. The data were normalized according to the maximal response of DAMGO.

(E–J) Size exclusion chromatography (SEC) profiles and SDS-PAGE analysis of μOR-Gi complexes bound with morphine (E), fentanyl (F), DAMGO (G), SR17018 (H), TRV130 (I), and PZM21 (J), respectively. For SR17018-μOR-G_i complex sample, a Superose 6 increase 10/300GL column was used for SEC purification, while for the other five μOR-G_i complex samples, a Superdex 200 increase 10/300GL column was applied.

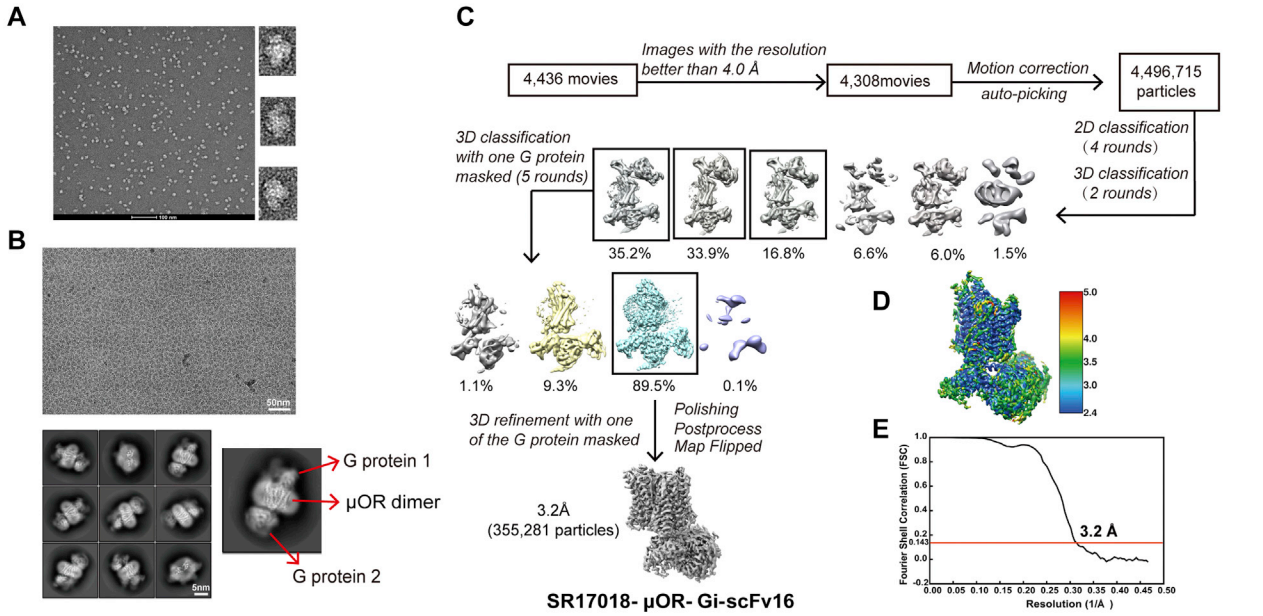

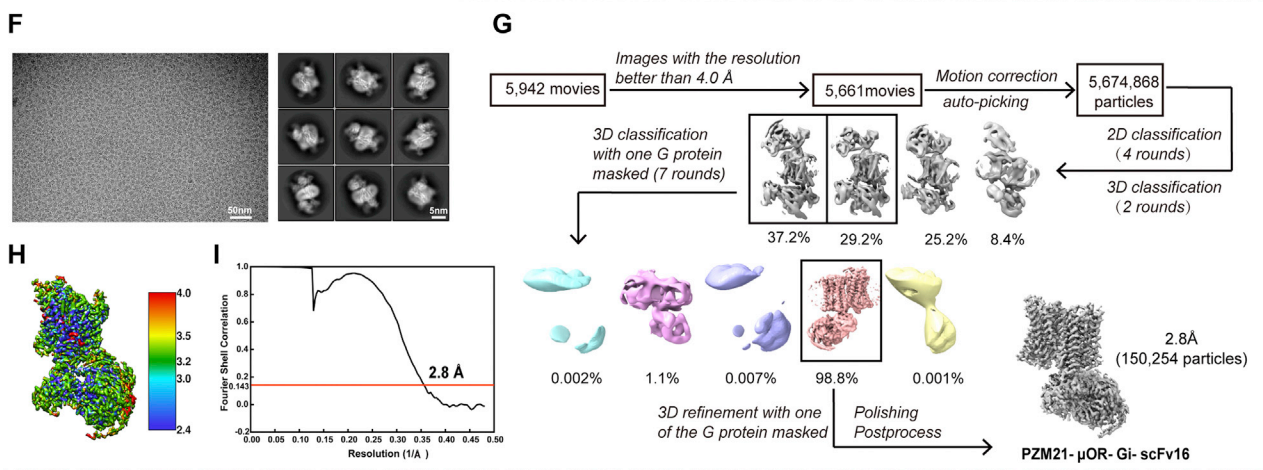

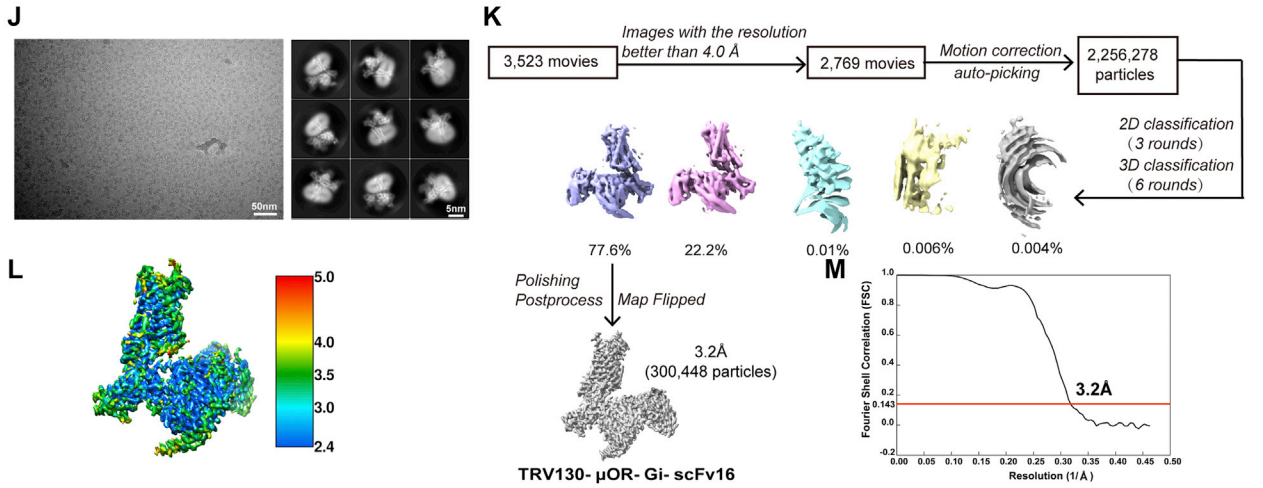

(legend on next page)

Figure S2. Structure determination of SR17018, PZM21, and TRV130 bound μOR-G_i complexes, related to Figure 1

(A) Representative negative staining image and particles of SR17018-μOR-G_i homodimer.

(B) Representative cryo-EM image and 2D classification averages of SR17018-μOR-G_i. The 2D averages show homodimers with anti-parallel conformations.

(C) Cryo-EM data processing flowcharts of SR17018-μOR-G_i by Relion 3.1.

(D) The Fourier shell correlation (FSC) curves of SR17018-μOR-G_i. The global resolution of the final processed density map estimated at the FSC = 0.143 is 3.2 Å.

(E) The global density map of SR17018-μOR-G_i colored by local resolutions, the density map is shown at a threshold of 0.023.

(F) Representative cryo-EM image and 2D classification averages of PZM21-μOR-G_i homodimer, the 2D averages show divergent secondary features of the homodimer with anti-parallel conformations.

(G) Cryo-EM data processing flowcharts of PZM21-μOR-G_i by Relion 3.1.

(H) The Fourier shell correlation (FSC) curves of PZM21-μOR-G_i. The global resolution defined at the FSC = 0.143 is 2.8 Å.

(I) The final global density map of PZM21-μOR-G_i colored by local resolutions, the density map is shown at 0.015 threshold.

(J) Representative cryo-EM image and 2D classification averages of TRV130-μOR-G_i complex, the 2D averages show divergent secondary features of protein conformations.

(K) Cryo-EM data processing flowcharts of TRV130-μOR-G_i by Relion 3.1.

(L) The Fourier shell correlation (FSC) curves of TRV130-μOR-G_i. The global resolution defined at the FSC = 0.143 is 3.2 Å.

(M) The final global density map of TRV130-μOR-G_i colored by local resolutions, the density map is shown a threshold of 0.027.

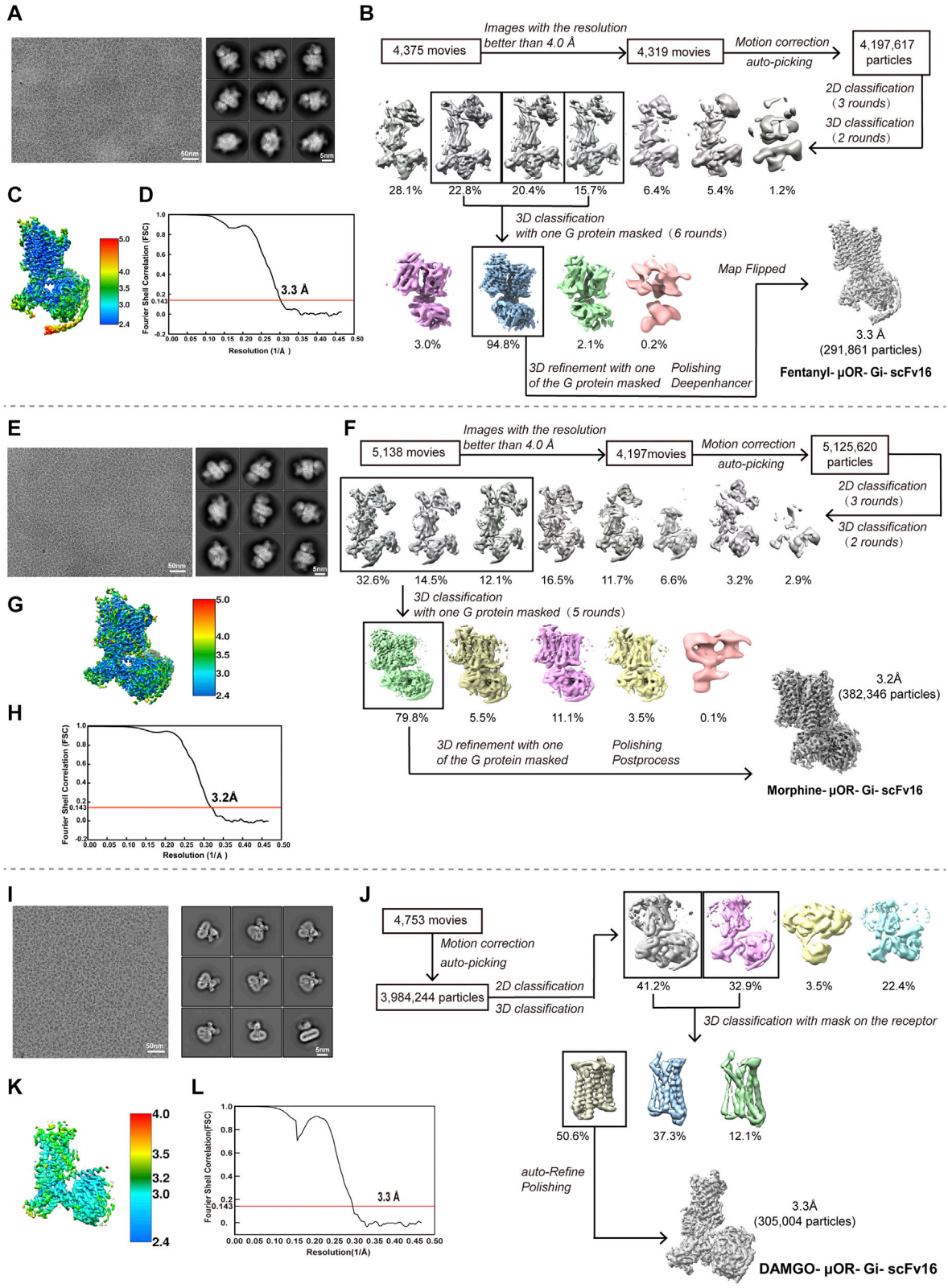

(legend on next page)

Figure S3. Structure determination of fentanyl, morphine, and DAMGO bound μOR-G_i complexes, related to Figures 1 and 2

(A) Representative cryo-EM image and 2D classification averages of fentanyl-μOR-G_i. The 2D averages show anti-parallel homodimers.

(B) Cryo-EM data processing flowcharts of fentanyl-μOR-G_i by Relion 3.1.

(C) The global density map of fentanyl-μOR-G_i colored by local resolutions, the density map is shown at threshold of 0.31.

(D) The Fourier shell correlation (FSC) curves of fentanyl-μOR-G_i. The global resolution of the final processed density map estimated at the FSC = 0.143 is 3.3 Å.

(E) Representative cryo-EM image and 2D classification averages of morphine-μOR-G_i homodimer, the 2D averages show divergent secondary features of the homodimer with anti-parallel conformations.

(F) Cryo-EM data processing flowcharts of morphine-μOR-G_i by Relion 3.1.

(G) The final global density map of morphine-μOR-G_i colored by local resolutions, the density map is shown at a threshold of 0.036.

(H) The Fourier shell correlation (FSC) curves of morphine-μOR-G_i. The global resolution defined at the FSC = 0.143 is 3.2 Å.

(I) Representative cryo-EM image and 2D classification averages of DAMGO-μOR-G_i complex, the 2D averages show divergent secondary features of protein conformations.

(J) Cryo-EM data processing flowcharts of DAMGO-μOR-G_i by Relion 3.1.

(K) The Fourier shell correlation (FSC) curves of DAMGO-μOR-G_i. The global resolution defined at the FSC = 0.143 is 3.3 Å.

(L) The final global density map of DAMGO-μOR-G_i colored by local resolutions, the density map is shown at a threshold of 0.791.

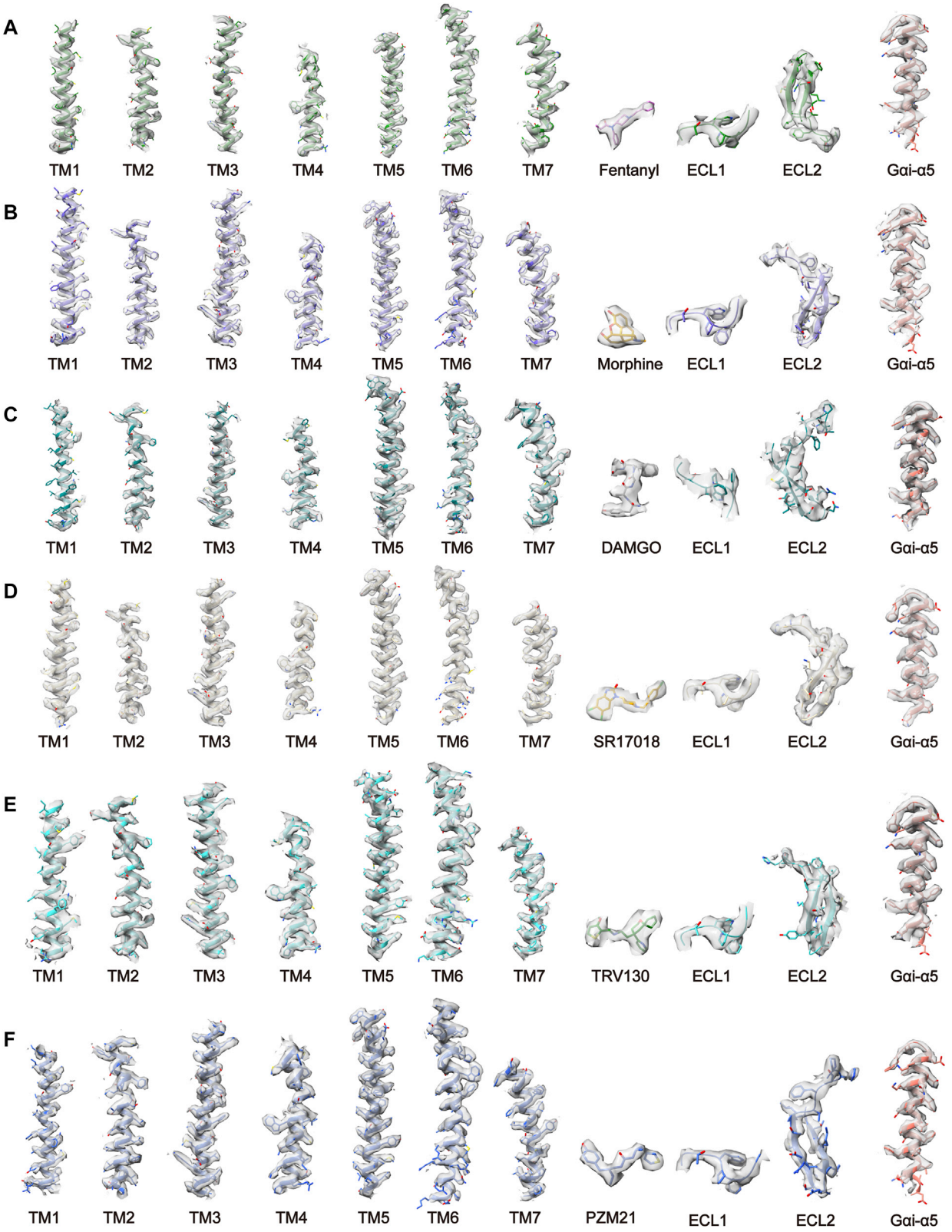

(legend on next page)

Figure S4. Local density maps of μOR-G_i signaling complexes, related to Figures 1 and 2

The density maps of helixes TM1–TM7 of transmembrane domain, extracellular loops ECL1/2 and helix 8 of μOR, α5 helix of $G_{\alpha i1}$, and opioid ligands in fentanyl (A), morphine (B), DAMGO (C), SR17018 (D), TRV130 (E), and PZM21 (F) bound μOR-G_i complexes, with thresholds shown at 0.197, 0.05, 0.512, 0.022, 0.017, and 0.015, respectively.

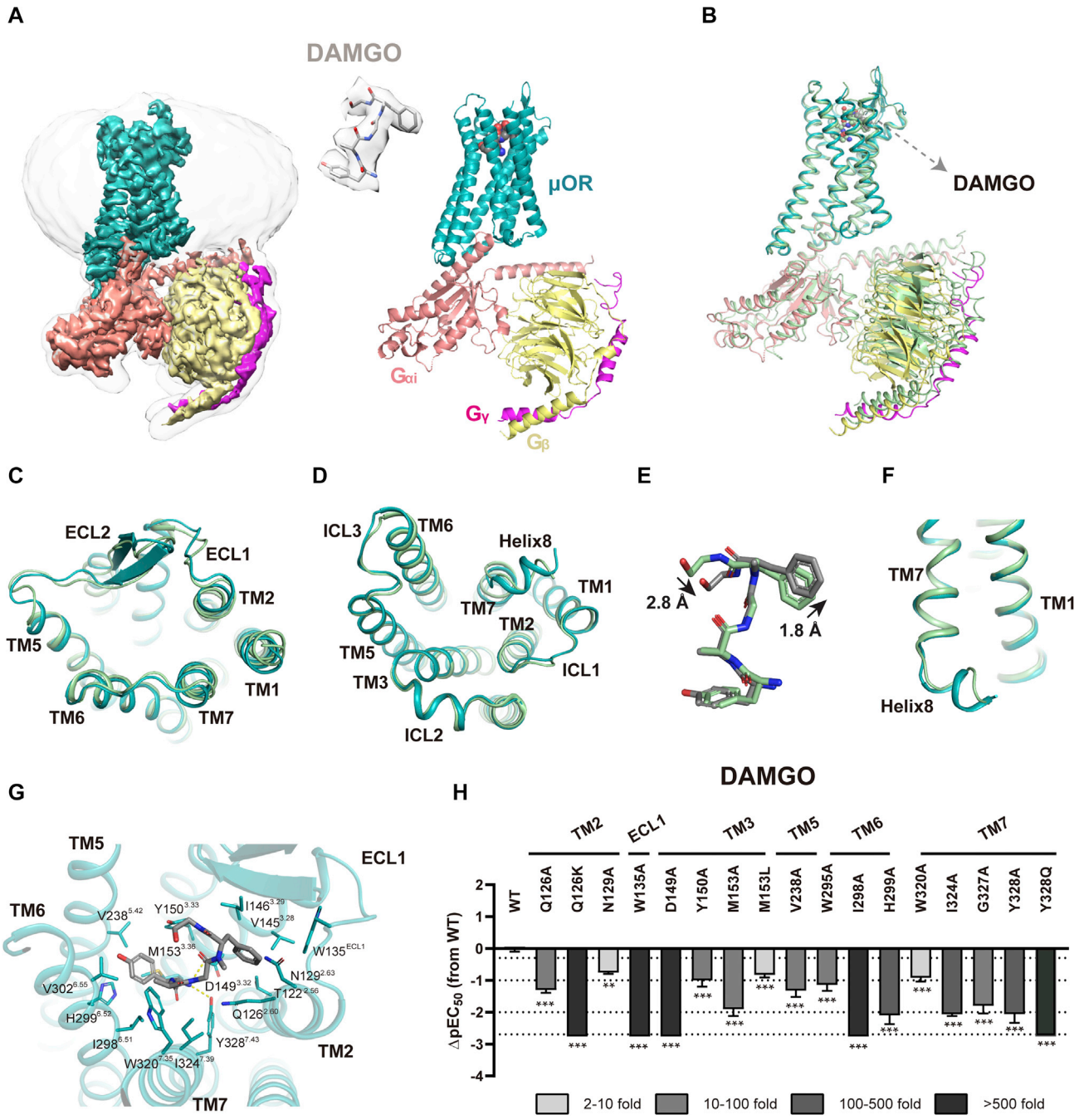

Figure S5. Differences between human- and mouse-derived DAMGO-μOR-G_i complexes, related to Figure 5

(A) Cryo-EM density map and molecular model of human DAMGO-μOR-G_i complex. Human μOR, teal; DAMGO, gray; $G_{\alpha i}$, salmon; G_β, light yellow; G_γ, magentas.

(B) Structural alignment of DAMGO bound human μOR-G_i complex and mouse μOR-G_i complex (PDB: 6DDF) structures. Human μOR, teal; DAMGO, gray; $G_{\alpha i}$, salmon; G_β, light yellow; G_γ, magentas. The whole DAMGO bound mouse μOR-G_i complex is colored in pale green.

(C–F) Comparison of the two DAMGO bound μOR-G_i complexes in extracellular region (C), intracellular region (D), the ligand pose (E), and conformation of helix 8 (F). Human μOR, teal; DAMGO, gray. The mouse DAMGO-μOR is colored in pale green.

(G) The interactions of DAMGO with human μOR. Human μOR, teal; DAMGO, gray.

(H) Effects of human WT μOR and μOR mutants in DAMGO induced cAMP accumulation. All data are presented as means ± SEM with a minimum of three independent replicates and each in triplicate. The significance was determined with two-side, one-way ANOVA followed by Fisher's LSD multiple comparisons test compared with WT. *$p < 0.05$; **$p < 0.01$; and ***$p < 0.001$ were considered as statistically significant.

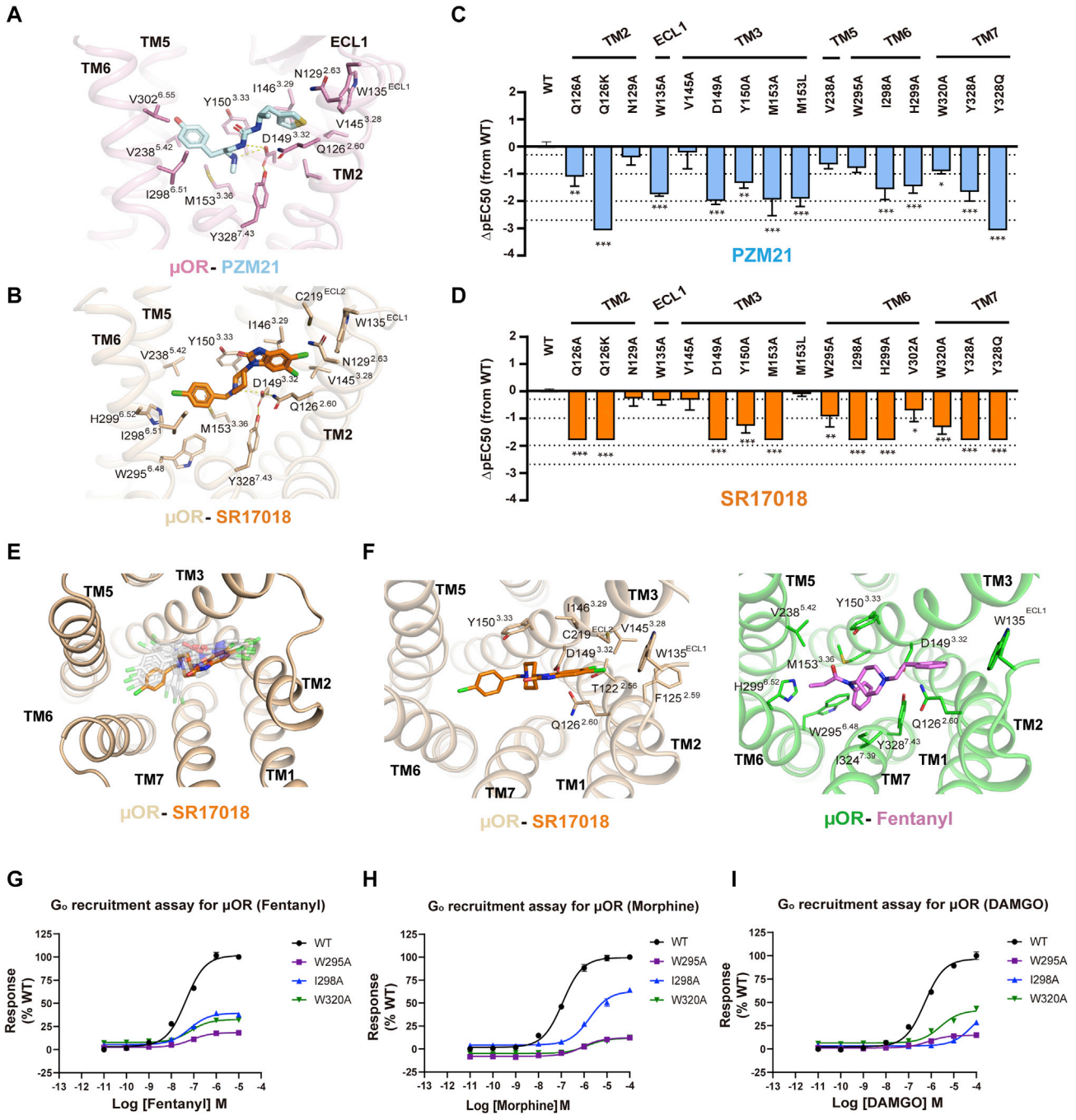

Figure S6. The binding profiles of PZM21, SR17018, and TRV130 to μOR, related to Figures 5 and 7

(A and B) Molecular interactions of PZM21 (A) and SR17018 (B) with residues around the μOR ligand-binding pocket. Both PZM21 and SR17018 have no direct interaction with TM7 residues. The hydrogen bonds are highlighted by yellow dashed lines.

(C and D) Validation of PZM21 (C) and SR17018 (D) binding by fluorescence resonance energy transfer (FRET) based cAMP accumulation assay. The value of each column indicated differences in potency (ΔpEC_{50}) of representative μOR mutants relative to the WT μOR. All data are presented as means ± SEM with a minimum of three independent replicates and each in triplicate. *$p < 0.05$; **$p < 0.01$; and ***$p < 0.001$ by one-way ANOVA followed by Fisher's LSD multiple comparisons test compared with WT.

(E) SR17018 binding poses during molecular dynamics simulations compared with the cryo-EM structure of SR17018-μOR. Opaque and translucent sticks show the SR17018 poses in cryo-EM structure and representative snapshots from molecular dynamics simulations, respectively. See also Video S1.

(F) The binding profile made up by residues which are in less than 4 Å distance to SR17018 or fentanyl in more than 40% of the trajectories. Residues with stable contacts are shown in stick representation.

(G–I) Effects of representative TM6/7 mutants, W295A, I298A, and W320A, on fentanyl (G), morphine (H), and DAMGO (I) activities in G_o recruitment assays. Data were presented as means ± SEM with a minimum of three technical replicates, which were performed in triplicates each.

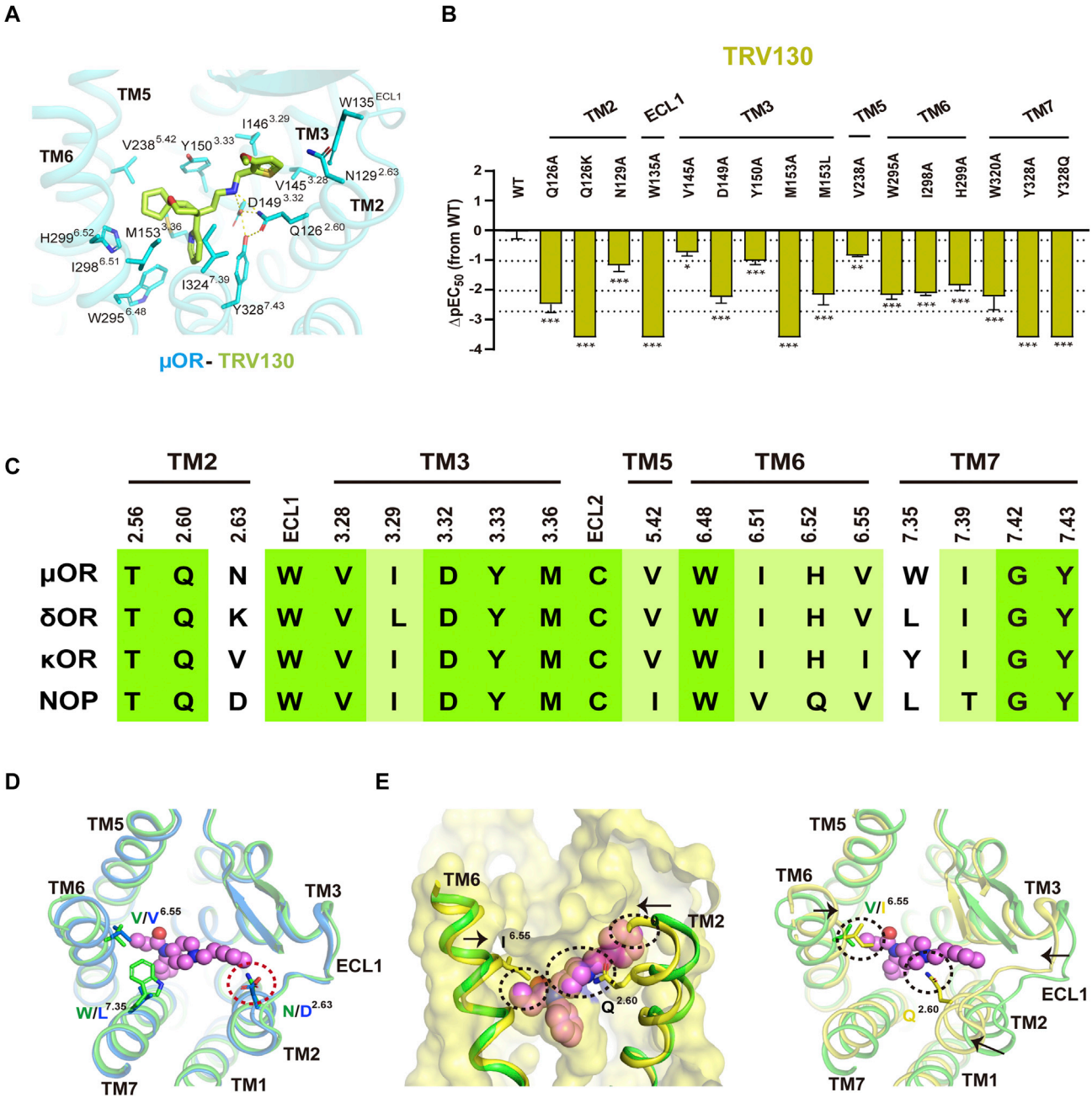

Figure S7. Selectivity of fentanyl toward μOR over δOR and κOR, related to Figures 2 and 5

(A) Molecular details of TRV130 with residues around the OBP of μOR.

(B) Validation of TRV130 binding by fluorescence resonance energy transfer (FRET) based cAMP accumulation assay. The value of each column indicates differences in potency (ΔpEC_{50}) of representative μOR mutants relative to the WT μOR. All data are presented as means ± SEM with a minimum of three independent replicates, each performed in triplicate. *$p < 0.05$; **$p < 0.01$, and ***$p < 0.001$ were considered as significant, the significance was determined by two-side, one-way ANOVA followed by Fisher's LSD multiple comparisons test compared with WT.

(C) Sequence alignment of residues in ligand-binding pockets of μOR, δOR, and κOR. The residue compositions in ligand-binding pockets of μOR, δOR, and κOR are highly conserved.

(D) A top view of fentanyl pose in aligned human μOR and active δOR (PDB: 6PT3) structures. The positive charged $K^{2.63}$ in δOR is energetically unfavorable for fentanyl binding. $K^{2.63}$ is mutated to aspartic in crystal structure of active δOR (PDB: 6PT3). Fentanyl is shown in spheres. μOR, green; δOR, marine; fentanyl, violet.

(E) The side view (left) and top view (right) of fentanyl binding pose in aligned human μOR and active κOR (PDB: 6B73) structures. The narrower κOR ligand-binding pocket induced by the inward movement of TM2/3/6 and ECL1 relative to μOR cause steric clashes with fentanyl. The steric clash regions are marked with dashed circles. The inward conformation changes are labeled with black arrows. Fentanyl is shown in spheres. μOR, green; κOR, yellow; fentanyl, violet.